Inter-laboratory Characterisation of Apatite Reference Materials for Chlorine Isotope Analysis

Alicja **Wudarska** (1, 2)* iD, Ewa **Słaby** (2), Michael **Wiedenbeck** (1), Jaime D. **Barnes** (3), Magali **Bonifacie** (4, 5), Neil C. **Sturchio** (6), Gérard **Bardoux** (4), Frédéric **Couffignal** (1), Johannes **Glodny** (1), Linnea **Heraty** (6), Timm **John** (7), Christof **Kusebauch** (1), Sathish **Mayanna** (1, 8), Franziska D. H. **Wilke** (1) and Ewa **Deput** (2)

(1) GFZ German Research Centre for Geosciences, Telegrafenberg, Potsdam 14473, Germany
(2) Institute of Geological Sciences, Polish Academy of Sciences, Research Centre in Warsaw, Twarda 51/55, Warsaw 00-818, Poland
(3) Department of Geological Sciences, University of Texas, Austin, TX, 78712, USA
(4) Institut de Physique du Globe de Paris, CNRS, Université de Paris, Paris F-75005, France
(5) Observatoire Volcanologique et Sismologique de Guadeloupe, Institut de Physique du Globe de Paris, Gourbeyre F-97113, France
(6) Department of Earth Sciences, University of Delaware, 255 Academy Street, Newark, DE, 19716, USA
(7) Institut für Geologische Wissenschaften, Freie Universität Berlin, Malteserstrasse 74-100, Berlin 12449, Germany
(8) Present Address: Carl Zeiss Microscopy GmbH, Carl Zeiss Straße 22, Oberkochen 73447, Germany
* Corresponding author. e-mail: ndgiera@cyf-kr.edu.pl

Here we report on a set of six apatite reference materials (chlorapatites MGMH#133648, TUBAF#38 and fluorapatites MGMH#128441A, TUBAF#37, 40, 50) which we have characterised for their chlorine isotope ratios; these RMs span a range of Cl mass fractions within the apatite $Ca_{10}(PO_4)_6(F,Cl,OH)_2$ solid solution series. Numerous apatite specimens, obtained from mineralogical collections, were initially screened for $^{37}Cl/^{35}Cl$ homogeneity using SIMS followed by $\delta^{37}Cl$ characterisation by gas source mass spectrometry using both dual-inlet and continuous-flow modes. We also report major and key trace element compositions as determined by EPMA. The repeatability of our SIMS results was better than $\pm$ 0.10‰ (1s) for the five samples with > 0.5% m/m Cl and $\pm$ 0.19‰ (1s) for the low Cl abundance material (0.27% m/m). We also observed a small, but significant crystal orientation effect of 0.38‰ between the mean $^{37}Cl/^{35}Cl$ ratios measured on three oriented apatite fragments. Furthermore, the results of GS-IRMS analyses show small but systematic offset of $\delta^{37}Cl_{SMOC}$ values between the three laboratories. Nonetheless, all studied samples have comparable chlorine isotope compositions, with mean $10^3\delta^{37}Cl_{SMOC}$ values between +0.09 and +0.42 and in all cases with 1$s \leq \pm$ 0.25.

Keywords: chlorine isotopes, apatite, matrix effect, crystal orientation effect, secondary ion mass spectrometry.

Chlorine isotopes in apatite-group minerals have gained attention due to advances in the secondary ion mass spectrometry technique (SIMS, e.g., Layne *et al.* 2004, Bouvier and Baumgartner 2013, Kusebauch *et al.* 2015a, Kusebauch et al. 2015b), which have enabled the investigation of the volatile elements in the solar system based on the chlorine isotope signatures found in small or heterogeneous apatite crystals from lunar (Sharp *et al.* 2010, Tartèse *et al.* 2014, Treiman *et al.* 2014, Boyce *et al.* 2015) and Martian materials (Sharp *et al.* 2016, Bellucci *et al.* 2017) as well as from smaller extra-terrestrial bodies such as Vesta

(Sarafian *et al.* 2017). In addition to extra-terrestrial studies, the halogen (F, Cl, Br, I) contents of apatite have been used to investigate element mobility and ore formation processes (e.g., Marks *et al.* 2012) and also to assess the extent of secondary alteration of apatite host rocks (Kusebauch *et al.* 2015a, Wudarska *et al.* 2020).

According to the IUPAC Technical Report (Brand *et al.* 2014) and following further recommendations for isotope data presentation by Coplen (2011) and Meisel (2019), the ratio of two stable chlorine isotopes ^{37}Cl and ^{35}Cl in a

sample should be expressed in relation to Standard Mean Ocean Chloride (SMOC) using Equation (1):

$$\delta^{37}Cl = \frac{{}^{37}Cl/{}^{35}Cl_{sample}}{{}^{37}Cl/{}^{35}Cl_{SMOC}} - 1 \qquad (1)$$

Moreover, it is recommended to report the relative difference of isotope ratios as $10^3\delta^{37}Cl$ rather than in commonly used per mil (‰) notation (Meisel 2019). In this manuscript, however, we used ‰ notation both to express measurement repeatability, which was calculated as relative standard deviation, and to report the difference in instrumental mass fractionation (IMF) in SIMS analyses. Furthermore, when quantifying the actual divergence of measured isotope ratios from the true values defined by gas source isotope ratio mass spectrometry (GS-IRMS), we used the widely employed notation:

$$\alpha_{inst.} = ({}^{37}Cl/{}^{35}Cl)_{meas.}/({}^{37}Cl/{}^{35}Cl)_{true} \qquad (2)$$

which is a unitless value directly related to the IMF induced bias according to:

$$IMF = (\alpha_{inst.} - 1) \times 1000 \qquad (3)$$

The anchor point for the $10^3\delta^{37}Cl_{SMOC}$ scale is +0.43 (Brand *et al.* 2014), which corresponds to the sodium chloride NIST SRM 975 (Xiao *et al.* 2002). However, due to the fact that the absolute ratio for this material $({}^{35}Cl/{}^{37}Cl = 3.1272)$ is associated with a significant uncertainty of $\pm$ 0.0082 (2*s*, Shields *et al.* 1963), throughout this paper we recalculated $\delta^{37}Cl_{SMOC}$ values obtained by GS-IRMS to ${}^{37}Cl/{}^{35}Cl$ ratios using the SMOC ratio of 0.319533 (zero point on the $\delta^{37}Cl_{SMOC}$ scale). This value was calculated based on the data reported for the sodium chloride secondary reference material (RM) ISL-354: $10^3\delta^{37}Cl_{SMOC}$ value of +0.05 $\pm$ 0.02 (1σ; Xiao *et al.* 2002) and ${}^{37}Cl/{}^{35}Cl$ ratio of 0.319549 $\pm$ 0.000044 (2*s*; Wei *et al.* 2012). The recalculation of $\delta^{37}Cl$ values obtained by conventional methods to ${}^{37}Cl/{}^{35}Cl$ ratios for our samples was necessary for quantifying the IMF of our SIMS analyses.

Most of the existing research on the chlorine isotope composition of geological materials has been based on bulk analyses using the GS-IRMS (e.g., Eggenkamp 1994, 2014). However, in those cases where limited amounts of material are available *in situ* analysis using SIMS is the method of choice. NanoSIMS instruments have proven useful for the analysis of lunar samples, where repeatability of measurements on the reference materials of ~ 1‰ is acceptable in view of the large natural variations of

$10^3\delta^{37}Cl_{SMOC}$ in lunar materials (from -1 up to +81, e.g., Sharp *et al.* 2010, Potts *et al.* 2018, Stephant *et al.* 2019, Wang *et al.* 2019). In contrast, the much narrower range of $\delta^{37}Cl$ values found in most terrestrial geological samples makes chlorine isotope ratio determinations challenging, both in terms of data acquisition and interpretation. Two recent studies of apatite crystals from Proterozoic and Archaean rocks have shown that chlorine isotope signatures of apatite can help in tracing metasomatic processes overprinting terrestrial rocks; such data can provide valuable information, despite displaying much narrower ranges of $10^3\delta^{37}Cl_{SMOC}$ values (from -1.2 to +3.8, Kusebauch *et al.* 2015a or from -0.8 to +1.6, Wudarska *et al.* 2020) compared with those recorded in the extra-terrestrial materials.

Quantitative isotope measurements by SIMS require homogeneous RMs of known isotope composition. Recent SIMS studies of $\delta^{37}Cl$ in apatite (Kusebauch *et al.* 2015a, Bellucci *et al.* 2017, Sarafian *et al.* 2017) have been based on two endmembers of the solid solution series represented by chemical formula $Ca_{10}(PO_4)_6(F,Cl,OH)_2$: natural fluorapatite from Durango (Mexico) and synthetic chlorapatite. A linear correction between IMF and Cl mass fraction was applied based on the analyses of these two materials (Kusebauch *et al.* 2015a). Unfortunately, these RMs are available only in small amounts. Taking into consideration the narrow range of chlorine isotope ratios in terrestrial materials, SIMS measurements require calibration using RMs closely matched to the chemical composition of the unknowns. Therefore, the goal of our current research was to develop a suite of well-characterised, homogeneous RMs covering a wide range of chlorine mass fractions in apatite making it possible to precisely define the matrix-dependent IMF of SIMS measurements. This issue has also been highlighted in the recent paper by Li *et al.* (2020) who concluded that additional RMs with a range of Cl mass fractions are required for routine $\delta^{37}Cl$ measurements, which would be in addition to a newly developed apatite RM (Eppawala-AP, Sri Lanka) described therein.

Previous SIMS isotopic works on magnetite, haematite and sphalerite showed that there may be a significant crystal orientation effect on measured oxygen and sulfur isotope ratios (Huberty *et al.* 2010, Kita *et al.* 2011). In view of the anisotropic behaviour of apatite during EPMA measurements (Stormer *et al.* 1993, Goldoff *et al.* 2012, Stock *et al.* 2015), which results from the incorporation of F⁻, Cl⁻ and OH⁻ in the anion column parallel to the *c*-axis of the hexagonal structure (Hughes and Rakovan 2002, Hughes *et al.* 2016), we also conducted a SIMS investigation of apatite fragments that were intentionally embedded in

epoxy mounts so as to provide differing crystallographic orientations.

Sample selection and description

A total of fifty-six natural apatite samples provided by mineralogical museums were tested for their chlorine isotope compositions ($^{37}Cl/^{35}Cl$) using SIMS. A suite of six specimens (Table 1, Figure 1, Appendix S1) that proved to be suitably homogeneous in $^{37}Cl/^{35}Cl$ (repeatability of measurements within ± 0.2‰, 1s) and representing a broad range of Cl mass fractions were further characterised using scanning electron microscopy-energy dispersive spectroscopy (SEM-EDS), EPMA, SIMS and GS-IRMS. Durango apatite, which is often used as a reference material in various analytical methods (e.g., McDowell et al. 2005, Teiber et al. 2015, Kusebauch et al. 2015a), has served in this study both as a test sample and as a quality control material. The six selected materials, previously cleaned in acetone and distilled water, were crushed and sieved to a grain-size fraction between 63 and 1400 μm (or in case of Durango between 63 and 1000 μm). These subsequently underwent mineral separation to remove any foreign phases and were finally split using a riffle splitter in order to generate multiple, metrologically identical units (Table 1). The purity of all split materials is estimated to be ≥ 98%.

MGMH#133648 consists of seven yellow-white crystals of chlorapatite from Norway, of which only the one fragment (~ 11.4 g) shown in Figure 1 was selected for this study, while the remaining material (~ 13.2 g) was returned to the Mineralogical and Geological Museum at Harvard University. A white crust of hydroxylapatite was removed from the surface of the chlorapatite crystal using a circular saw and a micro-drill. Crushed material underwent magnetic (Frantz) and heavy liquid (bromoform) separation. MGMH#133648 contains minor amounts of inclusions of hydroxylapatite, Ca-Mg-Fe-silicates and aluminosilicates, and calcite.

TUBAF#38 is a yellow crystal of chlorapatite from Bamble, Norway. A whitish grey crust of hydroxylapatite was removed from the surface of the chlorapatite crystal using a circular saw. Crushed material underwent magnetic (Frantz) and heavy liquid (bromoform) separation. TUBAF#38 contains minor amounts of inclusions of hydroxylapatite, Mg-silicates, Mg-Fe-Ca- and K-bearing aluminosilicates, and monazite.

TUBAF#40 is a green crystal of fluorapatite from Kragerø, Norway. Crushed material underwent magnetic (Frantz) and heavy liquid (bromoform) separation. TUBAF#40 contains minor amounts of inclusions of K- and Mg-aluminosilicates, Mg-silicates, monazite, quartz, calcite, Ca-sulfates and Fe-oxides.

MGMH#128441A is a yellow crystal of fluorapatite, which was selected for this study from eight specimens from Colorado, US; the other seven crystals, having similar Cl isotope compositions, were returned to the Mineralogical and Geological Museum at Harvard University. Dark-green mineral (possibly amphibole) was removed from the surface and from a cavity inside of the selected crystal using a micro-drill. Crushed material underwent magnetic (Frantz) separation. MGMH#128441A contains minor amounts of inclusions of Fe-oxides, Ca-Mg-Fe-Mn-silicates and aluminosilicates (some of which probably contain minor amounts of Cl), and monazite.

TUBAF#50 is a yellow, multi-crystal fluorapatite from Spain. Prior to crushing, the sample was hand-picked to remove non-apatite material (e.g., dust particles and contaminating fibres). TUBAF#50 is almost free from any inclusions; only a single inclusion of Fe-silicate was identified using SEM-EDS.

TUBAF#37 is a green fluorapatite from Bamble, Norway. Crushed material was treated with 12% acetic acid (in order to remove calcite) and the material then underwent further magnetic (Frantz) and heavy liquid (bromoform, diiodomethane) separation. TUBAF#37 contains minor amounts of inclusions of pyrite, quartz, calcite, Ca-Mg-silicates, Mg-Fe-aluminosilicates, Ba- and Ca-sulfates, and zircon.

Dur is a yellow fluorapatite from Durango, Cerro de Mercado, Mexico. A gem-quality single crystal contained only minor amounts of Fe-oxides, which could mostly be eliminated by careful hand-picking.

Analytical methods

Sample preparation

For further EPMA and SIMS characterisation, apatite crystals were mounted in epoxy resin in the centre of 25.4 mm diameter acrylic discs in which holes had been drilled. The mounts were subsequently polished to a < 5 μm surface quality as evaluated by white light interferometry. A total of five mounts were produced; they contained the following materials obtained from the splitting process described above:
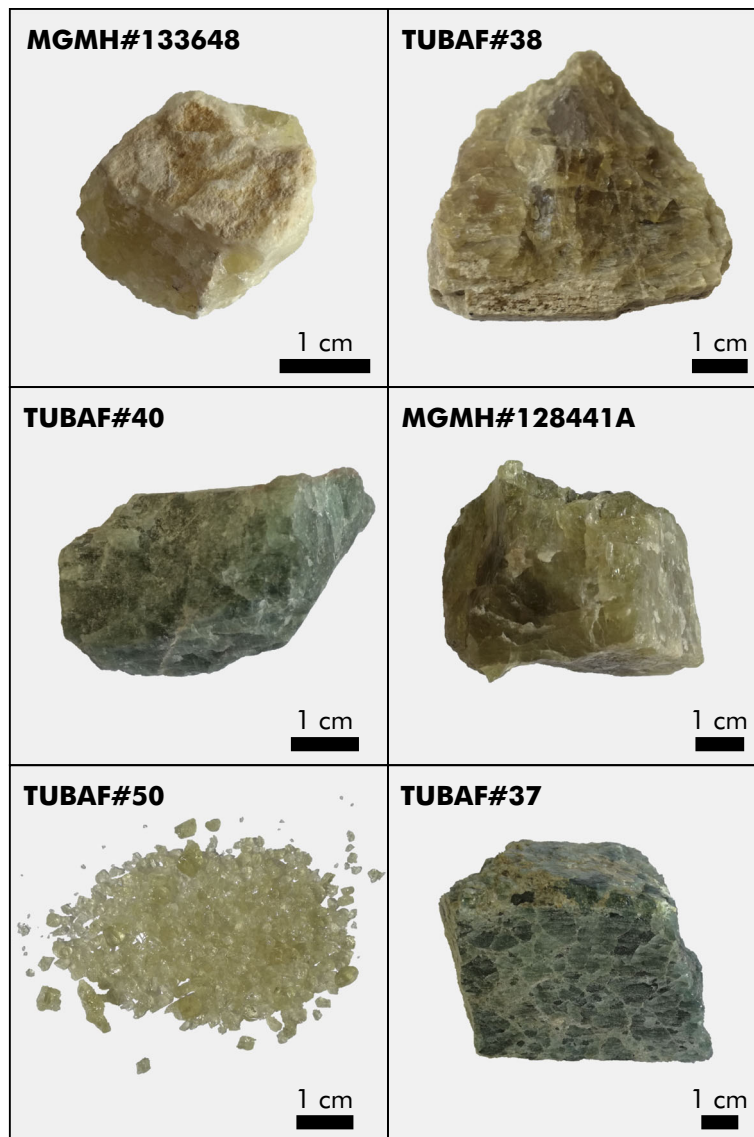
Figure 1. Photographs of the six apatite samples studied as provided by the mineralogical museums. [Colour figure can be viewed at wileyonlinelibrary.com]

● Mount #1: one unit of each sample (random crystals) and one fragment of both: the Durango apatite and the NIST SRM 610 silicate glass for tuning purposes (Figure 2).

● Mount #2: a few hand-picked crystals of TUBAF#37, which showed different hues of yellow colour under the binocular microscope, and a few crystals of TUBAF#38 having white, usually opaque, OH-enriched fragments (Appendix S2, Figure S2.1).

● Mount #3: a part of the white crust of hydroxylapatite mechanically removed from the surface of the MGMH#133648 sample (see section 'Sample selection and description'), which was embedded in epoxy to determine its isotopic composition, for addressing the minor amounts that we were unable to exclude from the sample splits (Appendix S2, Figure S2.2).

● Mount #4: three fragments of the Durango single crystal, which represent different orientations with respect to c-axis, along with a piece of NIST 610 glass for tuning purposes (Appendix S2, Figure S2.3).

● Mount #5: one unit of the Durango apatite (random crystals) for EPMA assessment only (Appendix S2, Figure S2.4).

Conventional $\delta^{37}Cl$ determinations in three independent GS-IRMS laboratories were performed on identical mineralogical splits that were hand-picked in Potsdam under a binocular microscope beforehand in order to remove most of the non-apatite material (minor amounts of inclusions were present in some analysed samples, but special attention was paid to remove any Cl-rich phases such as amphibole).

SEM-EDS and FE-SEM-EBSD analyses

Polished crystals embedded in epoxy as well as loose grains mounted on conductive carbon tabs were investigated at the Helmholtz Centre Potsdam (GFZ) using an Ultra Plus (Carl Zeiss, Oberkochen) field emission scanning electron microscope equipped with an EDS detector (Thermo Fisher Scientific) operated at 20 kV accelerating voltage in order to identify the chemical compositions of those phases associated with apatite samples.

The crystal orientations of the Durango apatite fragments selected for the assessment of crystallographic orientation effects on measured $^{37}Cl/^{35}Cl$ ratios were determined using

the electron backscatter diffraction technique (EBSD). Sample mount #4 (see above), which had been polished with silica colloid, was placed on a SEM stub using a carbon tape. EBSD point analyses and mapping (at 0.2 μm step size) were performed using a FEI Quanta 3D field emission scanning electron microscope equipped with an EBSD detector (AMETEK-EDAX Digiview 5 Camera) in low vacuum mode (~ 100 Pa) operated at 20 kV acceleration voltage and 23 nA beam current. The raw data were further processed using EDAX OIM software. The EBSD mapping results were filtered based on the Confidence Index (CI) and only the points having CI > 0.15 were taken into consideration for further interpretation.

Chemical analysis by EPMA

Quantitative chemical analyses of apatite crystals were performed using the JEOL Hyperprobe JXA-8500F microprobe at the GFZ. The samples were coated with a 20 nm thick carbon film and analysed for major and trace elements using an acceleration voltage of 15 kV, a spot size of 10 μm and two different beam current settings of 5 and 40 nA. Very low electron beam current of 5 nA and relatively large beam diameter were applied in order to minimise volatile (F, Cl) diffusion (Stormer *et al.* 1993, Goldoff *et al.* 2012), whereas a high electron beam current of 40 nA was used to detect REE and other trace elements. The details on the spectral lines, corresponding peak counting times and the calibration materials are given in Appendix S3. Calculations of the apatite formulae based on the EPMA data were performed using the method of Ketcham (2015) with normalisation done based on 25 oxygen equivalents. The OH content was calculated with the assumption that the X-site is fully occupied by F, Cl and OH (F + Cl + OH = 2).

Chlorine isotope homogeneity test by SIMS

In situ analyses of $^{37}Cl/^{35}Cl$ ratios were conducted using the Cameca 1280-HR large-geometry SIMS instrument at the GFZ. Prior to analyses, the sample mounts were cleaned in high-purity ethanol and were then argon sputter coated with a 35 nm thick high-purity gold film to assure electrical conductivity. A ~ 2 nA, nominally 10 keV $^{133}Cs^+$ primary ion beam focused to a ~ 5 μm diameter spot was used to produce $^{35}Cl^-$ and $^{37}Cl^-$ secondary ions following a modified protocol based on that of Kusebauch *et al.* (2015a). Using a 25 × 25 μm raster, the sample surface was sputtered for 60 s to remove the gold coat and to suppress surface contaminants. The raster was then reduced to a 15 × 15 μm, from which $^{35}Cl^-$ and $^{37}Cl^-$ secondary ions were collected simultaneously on Faraday cups, over twenty cycles with each
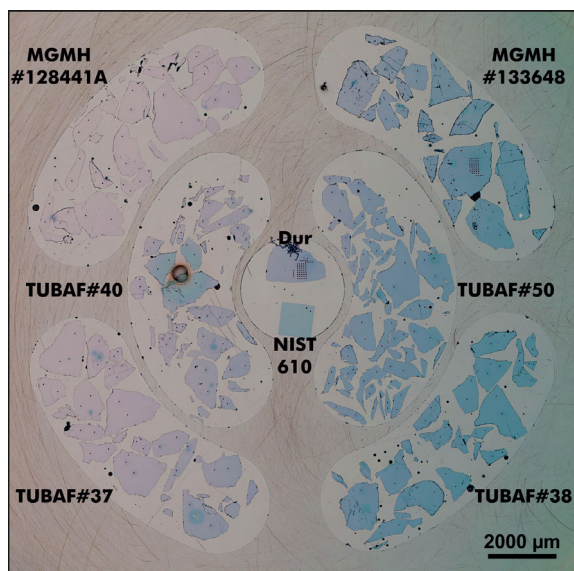
Figure 2. Reflected-light optical image of a gold-coated SIMS mount #1; image taken after completion of the SIMS $^{37}Cl/^{35}Cl$ measurements. Note the rectangular grid pattern on the Durango fragment (Dur) and on one of the MGMH#133648 grains where numerous analyses were conducted on a small area through the course of the analytical sequence. [Colour figure can be viewed at wileyonlinelibrary.com]

cycle lasting for 4 s. The mass resolving power (MRP) was $M/\Delta M \approx 1800$ (at 10% peak height).

According to earlier research on aluminosilicate glasses by Layne *et al.* (2004), a MRP of 5142 is necessary to separate adjacent peaks corresponding to $^{35}Cl^-$ and $^{34}S^1H^-$. Sulfur is commonly incorporated into the apatite structure (Pan and Fleet 2002); therefore, we have carefully developed our SIMS measurement protocol taking into consideration the risk of this potential interference. In the case of TUBAF#37, which has the lowest Cl/S ratio among all tested samples with $0.27 \pm 0.04\%$ *m/m* of Cl and $0.25 \pm 0.09\%$ *m/m* of SO_3, the $^{34}S^1H^-$ peak is nearly negligible (*ca.* 65 counts per second) in comparison with the very intense $^{35}Cl^-$ peak (*ca.* 3.15×10^5 counts per second, Figure 3). Hence, this added precaution seems worth considering only at very low Cl/S ratios during routine analyses.

The peak corresponding to $^{34}S^1H^-$ has been noted only using electron multiplier (EM) detection, while it could not be distinguished from the background of the Faraday cup (FC). Taking into consideration a very low intensity of this peak in EM detection, we have concluded that the isobaric interference of $^{34}S^1H^-$ with $^{35}Cl^-$ is irrelevant for our apatite homogeneity test, and therefore, we have conducted the measurements at a mass resolving power of ~ 1800 (Figure 4), which greatly improves ion counting rates leading to overall better data quality.

Multiple SIMS analysis points on multiple fragments were selected on all six apatite samples; these locations were broadly spaced and selected in a quasi-random fashion. Our SIMS data were collected in a single automatic, chain-analysis sequence that lasted ~ 17.5 h. Instrumental drift was monitored via closely spaced analyses both on the fragment of the Durango apatite and on one of the MGMH#133648 crystals that were regularly interspersed throughout the run. Additional tests of selected fragments of TUBAF#37, TUBAF#38 and MGMH#133648 embedded in two other mounts were conducted during the same session under identical analytical conditions. Three oriented fragments of the Durango apatite had been analysed a couple of months earlier following similar analytical protocol.

A typical count rate for $^{37}Cl^-$ ions was in the range from $\sim 3.8 \times 10^6$ (for fluorapatite TUBAF#37) to $\sim 9.4 \times 10^7$ (for chlorapatite MGMH#133648). The depth of sputtered sample pits was ~ 0.9 μm, and the amount of consumed material during each analysis was ~ 250 pg as based on

white light interferometry (for a 3D image of a typical SIMS crater, see Appendix S4).

Conventional $\delta^{37}Cl$ value determination by GS-IRMS

Isotopic studies can be affected by inter-laboratory bias, which results from differences in analytical protocols (e.g., Gonfiantini *et al.* 2003, John *et al.*, 2010, Manzini *et al.* 2017). In order to establish the extent of inter-laboratory bias for chlorine isotope measurements of apatite, conventional $\delta^{37}Cl$ values were determined independently in three gas source isotope ratio mass spectrometry laboratories. A traceability material of sodium chloride ISL-354 of known chlorine isotope composition ($^{37}Cl/^{35}Cl = 0.319549$, Wei *et al.* 2012; $10^3 \delta^{37}Cl_{SMOC} = +0.05$, Xiao *et al.* 2002) was analysed along with the apatite samples.

Dual-inlet isotope ratio mass spectrometry in laboratory 1: Chlorine isotope analyses at the Institut de Physique du Globe de Paris (France) were conducted using dual-inlet IRMS following the methods described in Eggenkamp (1994), improved by Godon *et al.* (2004), and used at IPGP ever since (e.g., Li *et al.* 2015, Eggenkamp *et al.* 2016, 2019). Apatite samples were fully dissolved in 15.5 ml of 4.4 mol l^{-1} HNO_3 and placed in an oven at 75 °C for ~ 7 h. All samples, except one (MGMH#133648), were independently dissolved twice (i.e., eleven separate dissolutions) before independent replicate preparation for $\delta^{37}Cl$ measurements ($n = 18$ in total). The amount of the processed material depended on the Cl concentration: from ~ 24 mg for chlorapatite MGMH#133648 up to ~ 360 mg for fluorapatite TUBAF#37. Chlorine was completely precipitated as AgCl after the addition of 5 ml of 1 mol l^{-1} $AgNO_3$. In contrast, following the recommendation of Eggenkamp (1994), for the precipitation of the internal seawater reference Atlantique 2 ($n = 10$) and of the international reference material ISL-354 (previously dissolved in ultrapure water; $n = 9$), we consecutively added: 4 ml of 1 mol l^{-1} KNO_3 (to increase the ionic strength of the solution), 2 ml of McIlvaine solution (to buffer solution at pH 2.2) and 1 ml of 0.2 mol l^{-1} $AgNO_3$.

After precipitation, AgCl was filtrated and protected from light on a 0.7 μm Whatman GF/F glass fibre filter. The filter was dried overnight in an oven at 80 °C and subsequently loaded into a Pyrex™ tube with excess of CH_3I, sealed under vacuum and reacted at 80 °C for 48 h. The tube was then cracked under vacuum, and the CH_3Cl was separated from the excess of CH_3I by gas chromatography (two columns filled with Porapak Q). The final amount of pure CH_3Cl generated was quantified by a capacitive gauge.
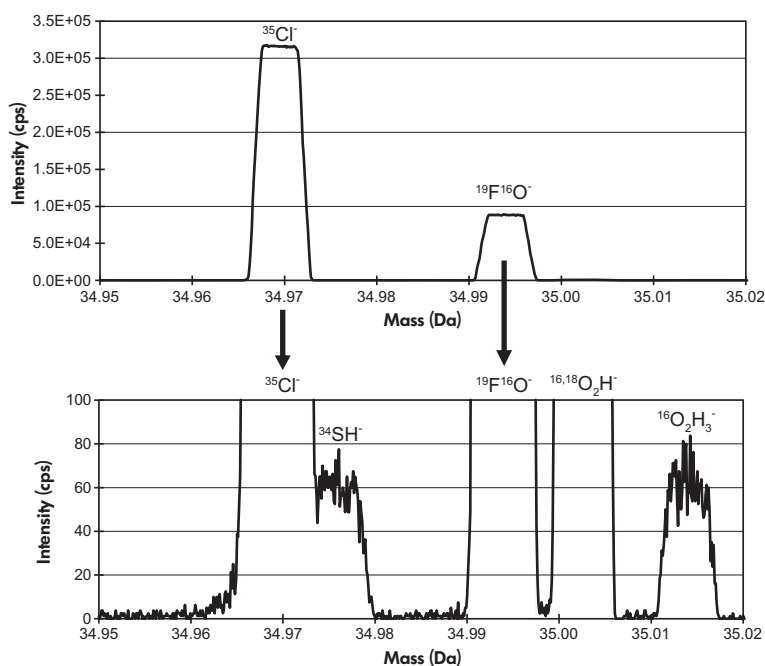
Figure 3. Secondary ion spectrum (registered using EM) at nominal mass of $^{35}Cl^-$ for the apatite sample TUBAF#37 illustrating isobaric interference with $^{34}S^1H^-$ at M/ΔM $\approx$ 5400 (at 10% peak height). Lower part of the figure shows a magnified spectrum from the upper part of this figure.
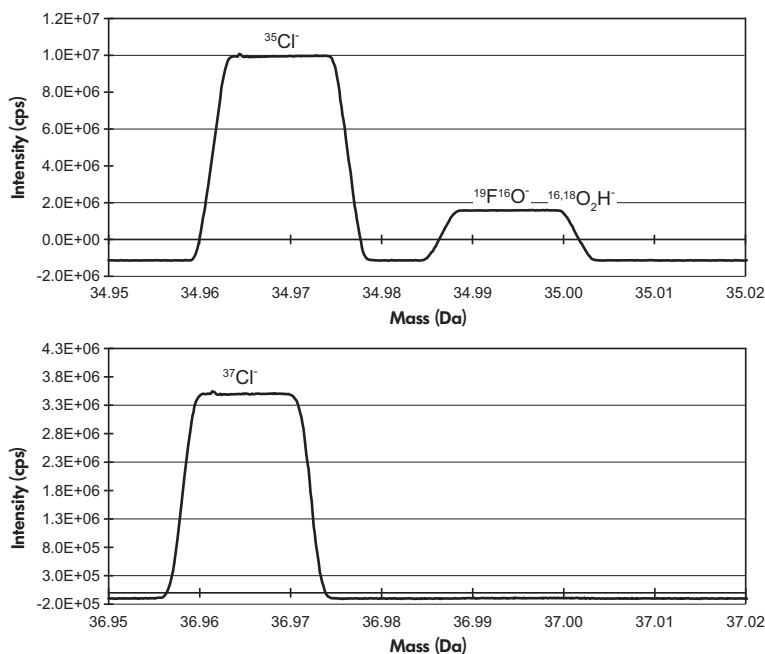
Figure 4. Secondary ion mass spectra (registered using FC) at nominal masses of $^{35}Cl^-$ and $^{37}Cl^-$ for the apatite sample TUBAF#37 at M/ΔM $\approx$ 1800 (at 10% peak height).

This provided a control of the quality of the whole procedure: apatite dissolution, AgCl precipitation, CH_3Cl fabrication and CH_3Cl purification. Yields for the whole procedure were calculated for each prepared aliquot of CH_3Cl, based on the mass of apatite dissolved and the results of EPMA measurements. Finally, CH_3Cl was collected in a sample

tube and transferred to a Thermo Scientific Delta V mass spectrometer.

All $\delta^{37}Cl$ measurements were normalised against at least two measurements of Atlantique 2 seawater [the internal seawater reference used by Godon et al. (2004) and since at IPGP] run each day under the same conditions of analyses as the apatite samples. All data were acquired on three consecutive days at IPGP. The uncertainty on each $10^3\delta^{37}Cl$ data is ± 0.04 (1s) based on long-term $\delta^{37}Cl$ measurements of Atlantique 2 (n = 150, and also checked on ten seawater analyses run over the course of this study). As a quality check for this normalisation, the $10^3\delta^{37}Cl$ values on nine aliquots of the reference material ISL-354 averaged -0.01 ± 0.10 (Table 5), which is consistent with the recommended value (+0.05, Xiao et al. 2002). To further check for the quality of the whole procedure for the $\delta^{37}Cl$ determination, we also ran five aliquots of seawater prepared with addition of $Na_2HPO_4 \cdot 2H_2O$ salt and concentrated HNO_3, and subsequently precipitated following the protocol used for the dissolved apatite samples (i.e., with the addition of $AgNO_3$ reactant only). The results of these tests are presented in Table S5.1 (Appendix S5). Total Cl amounts in all aliquots produced from the processed materials (the apatite samples and ISL-354) as well as in the reference seawater samples were within the range of 10–20 micromoles.

Finally, it is noteworthy that the calculated yields for the whole procedure (i.e., all steps of apatite dissolution, AgCl precipitation, CH_3Cl fabrication, CH_3Cl purification) averaged 99 ± 9% (Table S5.2 in Appendix S5), reflecting an excellent match between the Cl content estimated by EPMA with those measured based on apatite dissolution at IPGP.

Dual-inlet isotope ratio mass spectrometry in laboratory 2: Chlorine isotope analyses at the University of Delaware (USA) were conducted using dual-inlet IRMS. Each apatite sample was dissolved entirely (50–580 mg) in 0.5 mol l^{-1} HNO_3 at room temperature. Dissolutions were performed for two separate units of TUBAF#50, and a single dissolution was performed for one unit of each of the other samples. The reference materials ISL-354 and NIST SRM 975 were dissolved in ultrapure de-ionised water. Two or three replicate measurements of each sample and reference material were performed on separate aliquots of solution. The measurements were performed in two measurement sessions a year apart using two different mass spectrometers and applying additional steps in the sample preparation procedure in the second session.

Enough sample solution to yield between 10 and 30 micromoles Cl was aliquoted into a 50-cm³ centrifuge tube.

The aliquot volume was then adjusted to 10 ml by addition of ultrapure de-ionised water or by evaporation at 90 °C. Each adjusted sample aliquot was then further acidified with 200 μl of concentrated HNO_3 and then 3 ml of 1 mol l^{-1} $AgNO_3$ was added. Capped centrifuge tubes were warmed in a 90 °C oven for 30 min and then moved into a dark cabinet to cool and ripen overnight. AgCl solids were centrifuged at 2100 g for 3.5 min, and the supernatant solution was removed. The solids were rinsed three additional times with dilute HNO_3 followed by centrifugation. The solid AgCl was transferred into a pre-cleaned 9 mm diameter Pyrex combustion tube using a small section of a quartz fibre filter swab and small ultrapure water rinses. The AgCl was then evaporated to dryness at 90 °C in a dark oven.

The apatite sample TUBAF#37 produced unusual, superfine precipitates that did not separate from solution even after 20-min centrifugation. This sample was left in a dark cabinet for 8 months. The finally clear supernatant was removed and analysis by ion chromatography (IC) showed negligible chloride in solution. The solids were re-dissolved using two drops of concentrated NH_4OH and 10 ml deionised H_2O. The chloride concentration of this re-dissolved solution was comparable to the original raw solution. The re-dissolved TUBAF#37 solution was then re-acidified, and 3 ml of 1 mol l^{-1} $AgNO_3$ was added. The resulting precipitates were the expected AgCl solids. Aliquots of four other samples measured in the second session (MGMH#133648, MGMH#128441A, TUBAF#38 and TUBAF#40) and ISL-354 were also treated in the same manner.

Under vacuum, an excess of CH_3I (~ 200 micromoles) was cryogenically loaded into each combustion tube and sealed under vacuum with a methane-oxygen torch. Samples were then reacted at 300 °C for 2 h (Holt et al. 1997). The mixture of CH_3Cl and CH_3I was chromatographically separated with a 6 m ¼" PoraPlot packed column with helium carrier (70 ml min^{-1}, 65 °C). The CH_3Cl peak was monitored by a thermal conductivity detector and trapped using liquid nitrogen, while the CH_3I was back-flushed to waste and the helium carrier gas was pumped away.

In the first measurement session, the cryofocused CH_3Cl was directly expanded into the dual-inlet bellows of a Thermo Finnigan Delta Plus XL IRMS via a series of switching valves. In the second session, the CH_3Cl was cryogenically transferred into a 5-ml glass bulb with a PTFE HiVac valve. These samples were then manually introduced to the dual-inlet bellows of a Thermo Scientific Delta V-Plus IRMS the following day. The same reference CH_3Cl monitoring gas

was used for both mass spectrometers. The m/z 52/50 ratios of the sample gas were determined relative to this reference gas with its δ^{52} value set to 0.0. The ISL-354 reference material prepared along with the samples was used to calibrate results to the SMOC scale. The NIST SRM 975 reference sample was used as an additional quality control material (Table S5.3 in Appendix S5).

Continuous-flow isotope ratio mass spectrometry in laboratory 3: Chlorine isotope measurements at the University of Texas (Austin, USA) were conducted using continuous-flow isotope ratio mass spectrometry (CF-IRMS) following the methods outlined in Eggenkamp (1994) and modified by Sharp *et al.* (2007). Cl⁻ was extracted from approximately 15–100 mg of pre-weighed apatite via pyrohydrolysis, in which the sample was melted in the presence of an ultrapure de-ionised water vapour; Cl⁻ was then collected in 10 ml of 20 mmol l⁻¹ NaOH (Schnetger and Muramatsu 1996, Shimizu *et al.* 2015). Two separate pyrohydrolysis extractions were prepared for each sample. Reference material ISL-354 was dissolved in ultrapure de-ionised water, and separate aliquots were analysed from the same solution. Once the Cl⁻ was in solution, samples were prepared following the methods outlined in Eggenkamp (1994) and as described in detail above. The AgCl was reacted with excess CH_3I to produce CH_3Cl, which was purified on a column filled with Porapak Q and introduced into a Thermo Electron MAT 253. Measurements were calibrated against three seawater reference samples. Yields, based on sample peak areas compared with reference peak areas of known Cl contents, were 104 ± 25%. Cl amounts in all aliquots produced from the processed materials were within the range of ~ 0.8 to 2.4 micromoles. Samples were analysed during three separate measurement sessions.

This method's $10^3\delta^{37}Cl$ uncertainties during the measurement sessions were ± 0.13 (1s), which is slightly better than the laboratory's long-term uncertainty of ± 0.20 (1s). The solution leftovers from the halogen extraction via pyrohydrolysis were also analysed by IC at the GFZ in order to determine Cl mass fraction and to assess yields of the Cl extraction process. Method description and the results of the IC measurements are included in Appendix S5.

Results and discussion

Chemical composition

All apatite samples were investigated for their chemical composition using EPMA with two different electron beam current settings – 5 nA (Table 2) and 40 nA (Table 3) that

enabled us to obtain high-quality information on the mass fractions of both volatile (F, Cl) and trace elements, respectively. No zoning or margin-to-core chemical composition variations were detected on the random fragments of crushed material that were investigated. For full data sets of the individual EPMA measurements, see Appendix S6.

Selected apatite samples cover almost the full compositional space of the F-Cl-OH system (Figure 5) with the lowest Cl mass fraction determined for fluorapatite TUBAF#37 (0.27 ± 0.04% m/m, 1s) and the highest content in chlorapatite MGMH#133648 (6.34 ± 0.16% m/m, 1s). Due to volatile migration under electron beam influence (e.g., Goldoff *et al.* 2012), fluorine content was most probably overestimated in the data set obtained using 40 nA current, and therefore, further calculations of H_2O content by difference and the structural formulae were carried out using exclusively our 5 nA data set (Table 2). The chlorine mass fraction of MGMH#133648 varies notably depending on the electron beam current (median values are 6.34 ± 0.16% m/m (1s) and 6.09 ± 0.71% m/m (1s) for 5 and 40 nA, respectively). We observed grain-to-grain variations for MGMH#133648 (Appendix S6), which may suggest the crystal orientation effect previously noted in EPMA studies (e.g., Goldoff *et al.* 2012). Grain-to-grain variations were also observed for TUBAF#38, but Cl contents are similar with median values at 4.28 ± 0.12% m/m (1s) and 4.29 ± 0.19% m/m (1s) for 5 and 40 nA measurements, respectively. Both MGMH#133648 and TUBAF#38 contain OH-enriched areas identified in our SEM-based investigation of the inclusions, which could be the reason for grain-to-grain variations. It should be noted that these variations have not been detected in the 5-nA measurements, which were carried out at random locations on the very same crystal fragments as the 40 nA analyses. We note, however, that the sample mount was re-polished between the two sessions devoted to 5 and 40 nA measurements. Therefore, we advise using MGMH#133648 and TUBAF#38 with caution for chlorine abundance determinations due to a possible heterogeneous Cl/OH ratio in these two particular chlorapatite specimens.

The minerals of the apatite group can commonly incorporate different minor and trace elements into both cationic (e.g., La^{3+}, Ce^{3+}, Pr^{3+}, Nd^{3+}, Sr^{2+}, Mg^{2+}, Na^+) and anionic positions (e.g., SiO_4^{4-}, SO_4^{2-}, Pan and Fleet 2002). Accordingly, in the studied apatite samples various types and amounts of minor and trace elements were investigated. TUBAF#50 and MGMH#128441A are very rich in REEs, while MGMH#133648 and TUBAF#40 contain fewer such trace elements. Significant amounts of other components such as Sr, Mg and Na were detected in TUBAF#50. The

Table 1.
List of the apatite samples (in order of descending Cl mass fraction) used in this study

Sample ID	Source	Origin	Total mass (g)[a]	Number of splits
MGMH#133648	Mineralogical & Geological Museum at Harvard University	Norway, unknown locality	9.2	128
TUBAF#38	TU Bergakademie Freiberg	Bamble, Norway	73.9	512
TUBAF#40	TU Bergakademie Freiberg	Kragerø, Norway	20.0	128
MGMH#128441A	Mineralogical & Geological Museum at Harvard University	Colorado, US	84.0	512
TUBAF#50	TU Bergakademie Freiberg	Spain, unknown locality	4.5	32
Dur	Mineral dealer	Durango, Cerro de Mercado, Mexico	–	–
TUBAF#37	TU Bergakademie Freiberg	Bamble, Norway	207.8	1024

[a] Total masses of crushed apatite material produced after completion of mineral separation, which was subsequently split into metrologically identical units.

chemical composition of Dur (Durango, Mexico) closely matches the composition of other crystals from the same locality (e.g., Harlov and Förster 2003, Marks *et al.* 2012), which confirms the validity of the EPMA protocols applied in this study.

SIMS homogeneity test of ^{37}Cl/^{35}Cl ratios

The homogeneity test conducted on random apatite fragments from one unit of each sample (Figure 2) confirmed that they are sufficiently homogeneous at the sub-nanogram sampling scale in terms of their chlorine isotope composition. The repeatability precision of ≥ 30 measurements performed on a minimum of fifteen fragments was better than ± 0.2‰ (1s, i.e., 1 standard deviation) for all samples (Table 4, Figure 6, Appendix S7); in fact, it was better than ± 0.1‰ for all five samples having > 0.5% m/m Cl. All specimens were tested during the same measurement session under the identical conditions, and therefore, the measurements yielded better counting statistics and repeatability for Cl-rich samples. A mean uncertainty of single analysis determined for each sample was between ± 0.01‰ (1s) for chlorapatite MGMH#133648 and ± 0.11‰ (1s) for fluorapatite TUBAF#37 (Figure 6). Our instrumental drift monitor analyses interspersed periodically with analyses of the studied apatite samples showed that the data were collected under stable conditions, and therefore, no offline drift corrections were necessary.

Additional tests were conducted on hand-picked grains of TUBAF#37 and TUBAF#38, which looked visually different under the binocular microscope. A few grains representing yellow and colourless crystals of TUBAF#37 as well as milky and transparent crystals of TUBAF#38 (Appendix S2) were investigated using SEM-EDS and further analysed by SIMS

for their chlorine isotope compositions (Table 4, Figure 7, Appendix S7). BSE images collected for TUBAF#37 reveal that the yellow colouring results from a thin calcite layer, which covers some of the crystals, and which accordingly would have no impact on the ^{37}Cl/^{35}Cl ratios. Therefore, the chlorine isotope composition of yellow crystals in TUBAF#37 is consistent with the composition of colourless grains. Furthermore, SEM investigation showed that the white, usually opaque fragments of TUBAF#38 preserved traces of OH-replacement processes in this chlorine-rich sample. The ^{37}Cl/^{35}Cl ratios of OH-enriched areas determined by SIMS were measured and compared with the values collected for transparent, light-yellow crystals of TUBAF#38. This test showed only very small differences between the two crystal types (0.25‰ between two most extreme values; $n = 64$). In contrast, a similar test conducted on a piece of white crust removed from the surface of MGMH#133648 showed significant differences (up to 1.75‰, $n = 60$; Table 4, Figure 7, Appendix S7) between the most extreme value determined in OH-enriched area and the mean ^{37}Cl/^{35}Cl ratio for the volumetrically dominant, transparent, yellow crystals of MGMH#133648. The white crust was cut from the MGMH#133648 prior to crushing, but some minor amounts are still present in the split material. Therefore, we recommend that careful BSE and reflected-light optical observations of mounted polished crystals should be made prior to isotopic measurements so as to exclude any inclusions in all reference materials or OH-enriched areas in TUBAF#38 and MGMH#133648.

Crystallographic orientation effect on SIMS measured ^{37}Cl/^{35}Cl ratios

Minerals of the apatite group usually crystallise in the hexagonal crystal system (with space group $P6_3/m$), but

Table 2.
EPMA major element data for studied apatite samples, using 15 kV, 5 nA and 10 μm beam parameters

Sample ID	MGMH #133648		TUBAF#38		TUBAF#40		MGMH #128441A		TUBAF#50		TUBAF#37		Dur	
n	59		60		60		60		60		60		64	
	Med-ian	1s	Med-ian	1s	Med-ian	1s	Med-ian	1s	Med-ian	1s	Med-ian	1s	Med-ian	1s
P_2O_5	41.36	0.45	41.55	0.39	41.88	0.49	40.53	0.48	41.02	0.43	41.13	0.58	40.57	0.35
SiO_2	0.12	0.04	< DL		0.08	0.03	0.52	0.06	0.27	0.06	0.34	0.10	0.44	0.05
SO_3	0.09	0.04	0.10	0.04	0.07	0.04	0.11	0.04	0.08	0.04	0.25	0.09	0.32	0.07
CaO	54.21	0.46	54.20	0.52	55.16	0.53	53.47	0.63	52.77	0.47	55.29	0.54	54.82	0.40
SrO	0.09	0.04	< DL		< DL		0.04	0.03	0.90	0.08	0.26	0.04	0.06	0.04
FeO	< DL		0.16	0.06	< DL		0.09	0.06	< DL		< DL		< DL	
MnO	< DL		< DL		0.10	0.06	0.15	0.06	< DL		< DL		< DL	
Na_2O	0.07	0.05	0.19	0.05	0.06	0.04	0.18	0.05	0.36	0.07	0.03	0.03	0.21	0.05
F	< DL		0.44	0.12	1.70	0.17	2.15	0.13	3.38	0.17	3.22	0.13	3.45	0.19
Cl	6.34	0.16	4.28	0.12	1.40	0.11	0.99	0.08	0.55	0.07	0.27	0.04	0.47	0.05
H_2O	0.15	0.04	0.45	0.06	0.61	0.07	0.47	0.06	0.00	0.08	0.17	0.06	0.00	0.09
-O(F)	0.00		0.19	0.05	0.72	0.07	0.91	0.05	1.42	0.07	1.35	0.06	1.45	0.08
-O(Cl)	1.43	0.04	0.97	0.03	0.31	0.03	0.22	0.02	0.12	0.02	0.06	0.01	0.11	0.01
Total	100.99	0.76	100.22	0.70	100.02	0.82	97.56	1.01	97.79	0.71	99.54	0.88	98.78	0.60
Structural formulae $M_{10}(TO_4)_6X_2$														
Ca	9.93		9.91		9.97		9.89		9.75		10.03		10.03	
Sr	0.01		–		–		0.00		0.09		0.03		0.01	
Fe	–		0.02		–		0.01		–		–		–	
Mn	–		–		0.01		0.02		–		–		–	
Na	0.02		0.06		0.02		0.06		0.12		0.01		0.07	
$\sum M$	9.96		9.99		10.00		9.99		9.96		10.07		10.11	
P	5.99		6.00		5.98		5.93		5.99		5.89		5.86	
Si	0.02		–		0.01		0.09		0.05		0.06		0.08	
S	0.01		0.01		0.01		0.01		0.01		0.03		0.04	
$\sum T$	6.02		6.01		6.00		6.03		6.05		5.98		5.98	
F	–		0.24		0.92		1.17		1.84		1.72		1.86	
Cl	1.84		1.24		0.39		0.29		0.16		0.08		0.14	
OH	0.16		0.52		0.69		0.54		0.00		0.20		0.00	
$\sum X$	2.00		2.00		2.00		2.00		2.00		2.00		2.00	

< DL – below detection limit.
The data represent median values of between 59 and 64 individual measurements (*n*) conducted on a total of fifteen or sixteen fragments of each material. H_2O and OH components were calculated based on ideal stoichiometry. For the EPMA full data sets and the detection limits, see Appendix S6.

lowering of the symmetry is possible due to extensive cationic and anionic substitutions in the lattice (Hughes and Rakovan 2002). The apatite crystal structure parameters readily respond to the various content of the anion position, which is parallel to the *c*-axis of the hexagonal structure (e.g., Hughes *et al.* 2016). Accommodation of monovalent anions such as Cl⁻ and F⁻ in the anion column entails migration and exchange of these elements not only during the post-crystallisation processes, but also under the influence of the electron bombardment during the quantitative measurements by EPMA (Stormer *et al.* 1993, Goldoff *et al.* 2012, Stock *et al.* 2015). It has been shown that the crystallographic orientation of apatite has a significant effect on the time-dependent X-ray intensities of fluorine and chlorine (e.g., Goldoff *et al.* 2012). Furthermore, previous SIMS works

devoted to, for example, magnetite, haematite and sphalerite have also shown a significant crystal orientation effect on measured oxygen and sulfur isotope ratios (Huberty *et al.* 2010, Kita *et al.* 2011). Therefore, in this portion of our study three apatite fragments from a single crystal, but having differing orientations to the *c*-axis, were investigated by SIMS.

A portion of an euhedral crystal of the Durango fluorapatite was cut approximately perpendicular, parallel and slantwise (bevel cut) to the *c*-axis anion channel of the apatite structure. The orientation of these crystal fragments was confirmed by EBSD mapping (Figure 8), which showed that Dur-A is perpendicular to the *c*-axis and is close to the (0001) plane, Dur-B is parallel to the *c*-axis (close to the $(11\bar{2}0)$ plane), while Dur-C has an intermediate orientation.

GEOSTANDARDS and GEOANALYTICAL RESEARCH

Table 3.
EPMA major and trace element data for studied apatite samples, using 15 kV, 40 nA and 10 μm beam parameters

| Sample ID	MGMH #133648		TUBAF#38		TUBAF#40		MGMH #128441A		TUBAF#50		TUBAF#37		Dur	
n	45		45		45		45		44		45		45	
	Median	1s	Median	1s	Median	1s	Median	1s	Median	1s	Median	1s	Median	1s
P_2O_5	40.96	0.20	40.67	0.28	42.00	0.17	41.17	0.13	40.34	0.28	40.85	0.32	40.67	0.14
SiO_2	0.12	0.02	0.04	0.02	0.10	0.02	0.53	0.03	0.29	0.05	0.32	0.09	0.44	0.03
SO_3	0.11	0.02	0.14	0.02	0.11	0.02	0.19	0.02	0.13	0.02	0.34	0.11	0.30	0.05
Y_2O_3	< DL		< DL		< DL		0.10	0.02	< DL		< DL		0.05	0.01
La_2O_3	0.06	0.03	0.10	0.03	0.04	0.03	0.44	0.06	0.32	0.05	0.03	0.03	0.52	0.05
Ce_2O_3	0.14	0.04	0.27	0.04	0.11	0.03	0.89	0.08	0.89	0.08	0.11	0.04	0.69	0.04
Pr_2O_3	< DL		0.05	0.04	< DL		0.09	0.05	0.11	0.05	< DL		< DL	
Nd_2O_3	0.09	0.04	0.12	0.04	0.05	0.04	0.32	0.06	0.52	0.06	0.06	0.04	0.19	0.04
CaO	53.62	0.33	54.08	0.36	54.96	0.35	53.50	0.24	52.43	0.27	54.61	0.22	53.81	0.33
SrO	0.11	0.01	0.03	0.01	0.03	0.01	0.04	0.02	0.92	0.05	0.27	0.02	0.07	0.01
FeO	< DL		0.16	0.02	0.02	0.02	0.10	0.02	0.05	0.01	< DL		0.03	0.02
MnO	< DL		< DL		0.10	0.02	0.14	0.02	< DL		< DL		< DL	
MgO	< DL		0.04	0.01	< DL		0.04	0.01	0.36	0.04	< DL		< DL	
Na_2O	0.06	0.01	0.19	0.02	0.07	0.01	0.20	0.02	0.36	0.03	0.04	0.01	0.22	0.03
F	< DL		0.46	0.06	1.93	0.13	2.36	0.12	3.69	0.30	3.63	0.18	3.61	0.33
Cl	6.09	0.71	4.29	0.19	1.43	0.08	1.03	0.02	0.57	0.05	0.26	0.02	0.40	0.04
-O(F)	0.00	0.00	0.19	0.03	0.81	0.06	0.99	0.05	1.55	0.26	1.53	0.08	1.52	0.14
-O(Cl)	1.37	0.16	0.97	0.04	0.32	0.02	0.23	0.00	0.13	0.01	0.06	0.00	0.09	0.01
Total	100.00	0.77	99.48	0.29	99.81	0.46	99.91	0.36	99.29	0.41	98.93	0.40	99.39	0.49

< DL – below detection limit

The data represent median values of 44–45 individual measurements (n) conducted on fifteen fragments of each apatite sample. For the EPMA full data sets and the detection limits, see Appendix S6.

EBSD mapping of the Durango fragment cut slantwise to the c-axis channel (Dur-C) showed some variability in crystal orientation (visible as yellowish areas in the violet background in Figure 8). This is possibly an instrumental artefact related to the quality of the surface, but this interpretation needs further confirmation. Moreover, it was not possible to establish the Miller–Bravais indices for Dur-C due to the inconclusive results from EBSD point analyses; therefore, it is unclear which crystallographic plane is represented by the Dur-C fragment.

Repeatability of widely distributed SIMS analyses conducted on the individual oriented fragments was in all three cases better than ± 0.09‰ (1s, n = 10–18; Table 4, Appendix S7), proving their internal homogeneity, while the repeatability of the measurements of all three fragments was ± 0.16‰ (1s, n = 38). For the Cameca 1280-HR SIMS instrument operated at primary and secondary accelerating voltages of +10 and -10 kV, respectively, the incident Cs^+ beam angle is 21° from the normal to the sample surface (Huberty et al. 2010). Consequently, during the measurements of Dur-A and Dur-B the incident primary beam angle was about 20° and 70° from the c-axis channel,

respectively. The SIMS analyses yielded higher (by 0.16%) $^{37}Cl/^{35}Cl_{measured}$ ratios for Dur-A (0.32072 ± 0.00002, 1s) compared with the ratios measured in Dur-B
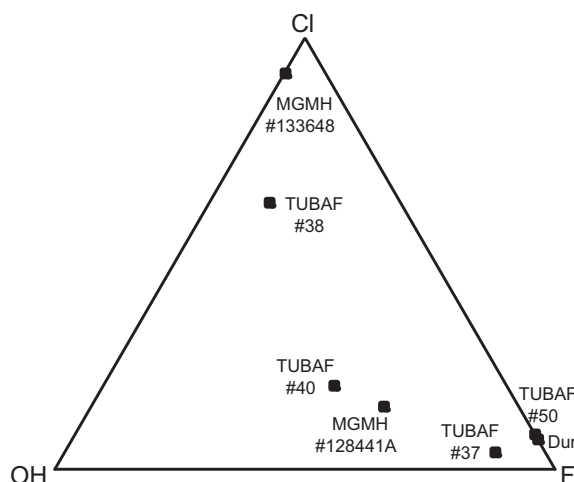
Figure 5. Ternary plot showing median F-Cl-OH compositions of the studied samples determined by EPMA (Table 2).

Table 4.
Results of SIMS homogeneity tests

Sample ID	Number of fragments	Number of analyses	Measured ^{37}Cl/^{35}Cl ratios[a]			Repeatability 1s [‰]		Mean $10^3\delta^{37}$Cl$_{SMOC}$ ± 1s[b]
			Range	Mean	1s (abs)			
Randomised analyses on random crystals (13–14.02.2018)								
MGMH#133648	17	33	0.32017–0.32020	0.32019	0.00001	0.02		0.10 ± 0.02
MGMH#133648[c]	1	43	0.32013–0.32020	0.32019	0.00001	0.04		0.09 ± 0.04
TUBAF#38	17	34	0.32018–0.32024	0.32022	0.00002	0.05		0.11 ± 0.05
TUBAF#40	18	36	0.32027–0.32034	0.32031	0.00002	0.05		0.23 ± 0.05
MGMH#128441A	15	30	0.32029–0.32040	0.32036	0.00002	0.06		0.36 ± 0.06
TUBAF#50	25	50	0.32028–0.32042	0.32033	0.00003	0.10		0.26 ± 0.10
TUBAF#37	15	30	0.32020–0.32049	0.32030	0.00006	0.19		0.14 ± 0.19
Dur-1[c]	1	43	0.32028–0.32042	0.32036	0.00003	0.10		0.34 ± 0.10
Randomised analyses on the selected crystals (14.02.2018 and 15.02.2018)								
TUBAF#37-A	10	20	0.32016–0.32031	0.32024	0.00005	0.15		0.09 ± 0.15
TUBAF#37-B	12	27	0.32014–0.32036	0.32025	0.00005			0.12 ± 0.15
TUBAF#38-A	13	30	0.32013–0.32021	0.32017	0.00002	0.04		0.08 ± 0.05
TUBAF#38-B	17	34	0.32016–0.32019	0.32017	0.00001			0.08 ± 0.02
Dur-2[c]	1	28	0.32022–0.32037	0.32029	0.00005	0.14		0.27 ± 0.14
MGMH#133648-A	1	26	0.32014–0.32071	0.32026	0.00019	0.41		0.40 ± 0.58
MGMH#133648-B	17	34	0.32014–0.32017	0.32015	0.00001			0.07 ± 0.03
Dur-3[c]	1	17	0.32025–0.32041	0.32032	0.00004	0.12		0.19 ± 0.12
Randomised analyses on the oriented crystals (20.06.2017)								
Dur-A	1	10	0.32068–0.32075	0.32072	0.00002	0.06		0.20 ± 0.06
Dur-B	1	18	0.32060–0.32073	0.32067	0.00003	0.09	0.16	0.06 ± 0.09
Dur-C	1	10	0.32075–0.32082	0.32079	0.00002	0.06		0.41 ± 0.06

For full data sets of all individual SIMS analyses, see Appendix S7.

[a] Not corrected for IMF.

[b] The data collected in February 2018: $10^3\delta^{37}$Cl$_{SMOC}$ values were calculated based on the correlation of α_{inst} with Cl concentration (for further details, see Figure 10 and subsection 'Matrix effect and IMF'). The data collected on the oriented crystals in June 2017: $10^3\delta^{37}$Cl$_{SMOC}$ values were calculated based on the α_{inst} determined using the mean ^{37}Cl/^{35}Cl ratio for Dur-A, Dur-B and Dur-C. The data reduction for all measurements was conducted using the absolute SMOC ^{37}Cl/^{35}Cl ratio of 0.319533 (zero point on the δ^{37}Cl$_{SMOC}$ scale; see the third paragraph of Introduction for further details).

[c] Instrumental drift monitor analyses regularly interspersed with analyses of the studied apatite samples. Dur-1, Dur-2 and Dur-3 indicate three randomly oriented fragments of the Durango apatite, which were used for monitoring the instrumental drift.

(0.32067 ± 0.00003, 1s). This further suggests that interaction of the primary Cs$^+$ beam with the chlorine ions in the apatite channel enhances mobility of the heavier isotope ^{37}Cl. The difference between the mean ^{37}Cl/^{35}Cl ratios calculated for the parallel (Dur-B) and the intermediate (Dur-C; ^{37}Cl/^{35}Cl$_{measured}$ = 0.32079 ± 0.00002, 1s) members is even greater: they differ by 0.38‰. Taking the mean ^{37}Cl/^{35}Cl ratio of 0.32071 ± 0.00005 (1s) for all three crystal fragments and the recommended $10^3\delta^{37}$Cl$_{SMOC}$ value of +0.19 ± 0.07 for Durango apatite (Table 5), the corresponding $10^3\delta^{37}$Cl$_{SMOC}$ values for each individual crystal are as follows: +0.20 ± 0.06 (Dur-A), +0.06 ± 0.09 (Dur-B) and +0.41 ± 0.06 (Dur-C). Despite the fact that the exact angle between the primary beam and the crystallographic plane represented by Dur-C could not be established, this test shows that there is a significant crystallographic orientation effect on ^{37}Cl/^{35}Cl ratios

measured in apatite, which should be taken into consideration during future SIMS works.

Conventional δ^{37}Cl values

Conventional analyses (GS-IRMS) of stable chlorine isotopes have been successfully applied to various geological materials, mostly fluids, silicates and salts (e.g., Godon et al. 2004, Sharp et al. 2007, Bonifacie et al. 2007, Li et al. 2015, Eggenkamp et al. 2019). GS-IRMS data for the minerals of the apatite group are scarce (e.g., Kusebauch et al. 2015c), and the impact of choices made when designing an analytical protocol has not previously been established.

All apatite samples investigated in this study have comparable chlorine isotopic compositions to the mean
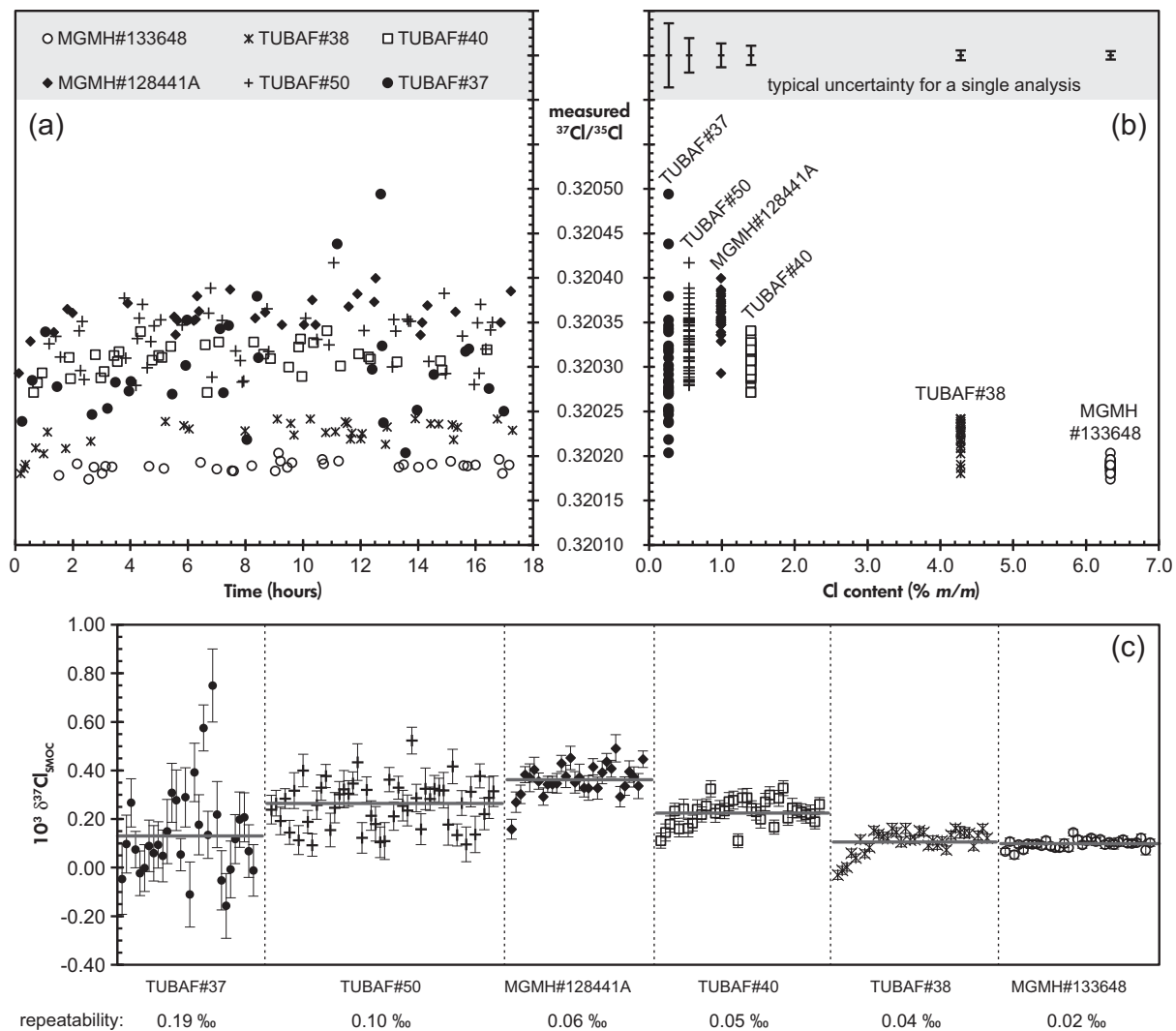
Figure 6. (a, b) Individual $^{37}Cl/^{35}Cl$ measurements by SIMS (not corrected for IMF). (a) The data were collected under stable conditions in a single automatic, chain-analysis sequence that lasted ~ 17.5 h. An offline correction for instrumental drift was unnecessary. (b) Repeatability of SIMS analyses was better than 0.10‰ (1*s*) for all five samples having more than 0.5% *m/m* of Cl (TUBAF#50, MGMH#128441A, TUBAF#40, TUBAF#38, MGMH#133648), and 0.19‰ for the low Cl abundance apatite TUBAF#37. The range bars represent a typical within-run 1*s* uncertainty for each material; they decrease from ± 0.11‰ for fluorapatite TUBAF#37 to ± 0.01‰ for chlorapatite MGMH#133648. (c) SIMS $10^3\delta^{37}Cl$ values were calculated based on a correlation of IMF factor with Cl mass fraction. For further details, see Figure 10 and subsection 'Matrix effect and IMF'. The uncertainty bars represent within-run 1*s* uncertainty for each data point, and the grey lines represent weighted means for each material.

$10^3\delta^{37}Cl_{SMOC}$ values clustering between +0.09 and +0.42, which is in contrast to a wider range of values represented by the two reference samples – Durango (+0.5) and synthetic chlorapatite (+2.0) – characterised by Kusebauch *et al.* (2015a) or the Norwegian samples studied therein which span a range from -1.2 up to +3.7. Determined $10^3\delta^{37}Cl_{SMOC}$ values do not correlate with Cl mass fractions (Table 5, Figure 9). There are significant

differences between individual data sets generated in three independent GS-IRMS laboratories. The offset of $10^3\delta^{37}Cl_{SMOC}$ values is not constant for all studied specimens, and it varies from 0.05 to 0.67. However, the values determined at the UT Austin are generally the highest, whereas those measured in IPGP are usually the lowest and the values reported by the Delaware laboratory in most cases fall between the data provided by the other two
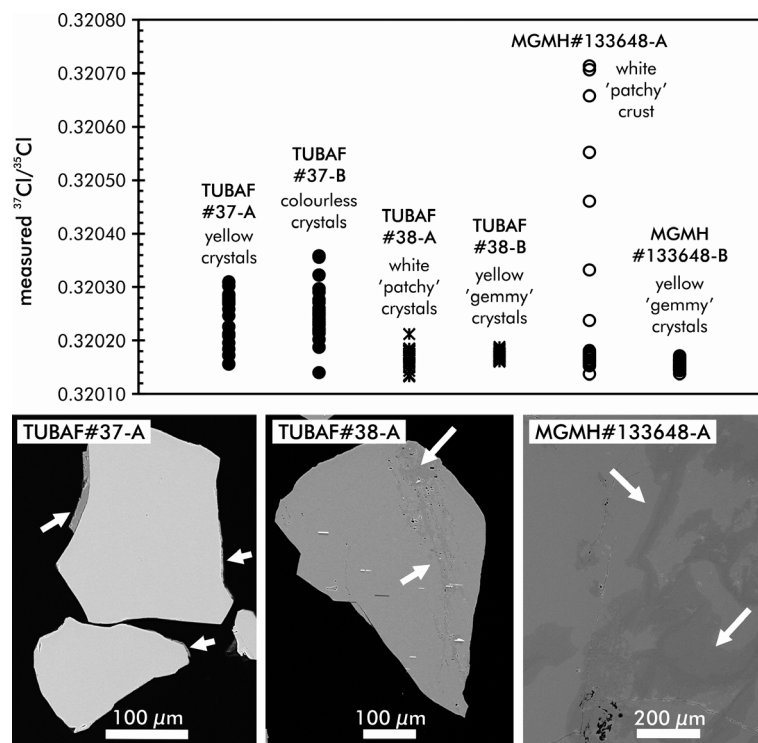
Figure 7. $^{37}Cl/^{35}Cl$ ratios measured using SIMS (not corrected for IMF) on hand-picked apatite crystals of TUBAF#37 and TUBAF#38 (see Figure S2.1) as well as on a piece of white crust of hydroxylapatite mechanically removed from the surface of MGMH#133648 (Figure S2.2). In lower panels, the arrows on the BSE images indicate anomalous material present in TUBAF#37-A (a thin carbonate layer on the apatite crystals), TUBAF#38-A (OH-enriched veins) and MGMH#133648-A (OH-enriched areas in the crust).

laboratories. In contrast, for all three GS-IRMS laboratories the $10^3\delta^{37}Cl_{SMOC}$ values determined for sodium chloride ISL-354 are in close agreement with the published value of +0.05 (Xiao *et al.* 2002), which confirms that the analytical protocols for silver chloride precipitation and measurement were developed and applied properly in all three laboratories.

In general, continuous-flow IRMS determinations combined with pyrohydrolysis are characterised by higher uncertainty ($\pm$ 0.20 for UT Austin) than those conducted in dual-inlet IRMS mode combined with dissolution in HNO_3 ($\pm$ 0.04 for both IPGP and U. Delaware). This results not only from the principles of these two methods, but also from the fact that Cl concentrations in all aliquots produced from the processed materials via pyrohydrolysis (from ~ 0.8 to 2.4 micromoles) were significantly lower than those obtained via apatite dissolution in HNO_3 (10–30 micromoles). The offset between laboratories is not observed for the sodium chloride ISL-354, but it should be noted that this reference material did not undergo pyrohydrolysis and was dissolved in de-ionised water in all three laboratories. This could further

suggest that the process of pyrohydrolysis may have had a significant role regarding the variations in the determined $\delta^{37}Cl_{SMOC}$ values. However, the ion chromatography measurements conducted on the solution leftovers from the halogen extraction via pyrohydrolysis showed that Cl concentrations in the solutions produced from the apatite samples match the compositions determined by EPMA (Appendix S5, Table S5.4). In the case of the Cl-poor fluorapatite samples, the estimated yields are lower (e.g., 83–86% for TUBAF#37) compared with the yields for chlorapatite samples (e.g., 94–96% for MGMH#133648), but these differences do not correlate with the offsets between laboratories.

Furthermore, a set of seawater aliquots were prepared at IPGP with the addition of $Na_2HPO_4 \cdot 2H_2O$ and HNO_3; the IRMS measurements yielded a mean $10^3\delta^{37}Cl_{SMOC}$ value of -0.05 $\pm$ 0.04 (1s; Appendix S5, Table S5.1), which is in very good agreement with the value for seawater (SMOC, $10^3\delta^{37}Cl$ = 0; Brand *et al.* 2014). This suggests no influence of the phosphate matrix on the precipitation of AgCl and measured chlorine isotope compositions.
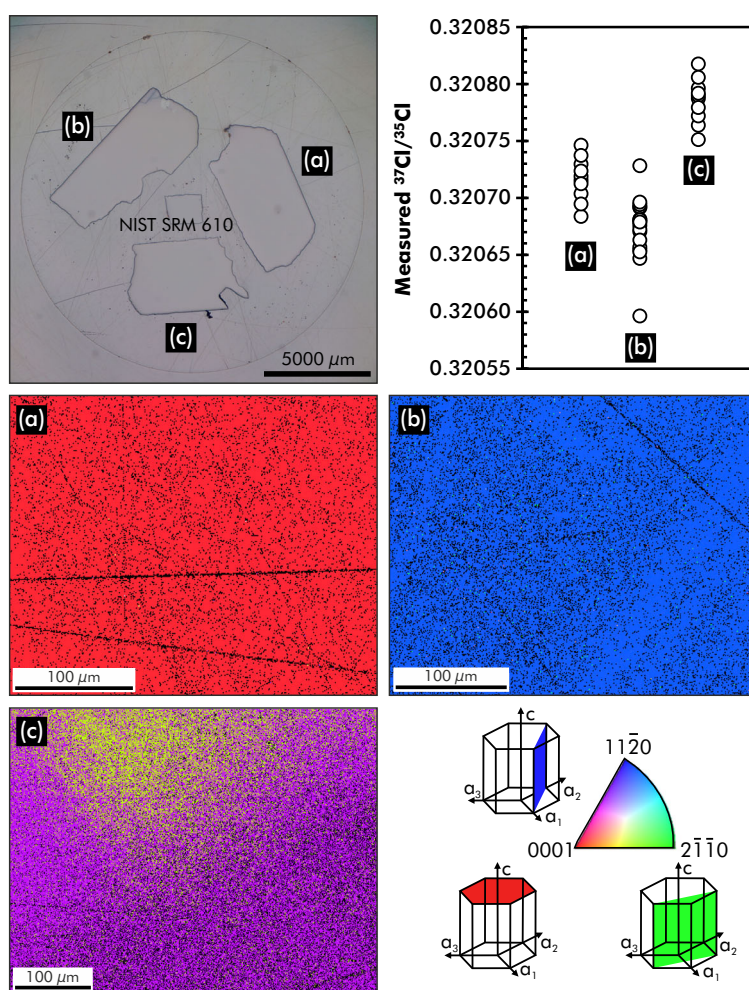
Figure 8. Results of crystal orientation test of three Durango apatite fragments having different crystal orientation with respect to the *c*-axis. EBSD maps showed that Dur-A (red) is perpendicular to the *c*-axis and is close to the (0001) plane, Dur-B (blue) is parallel to the *c*-axis (close to the $(11\bar{2}0)$ plane), while Dur-C (violet) has an intermediate member. The mean $^{37}Cl/^{35}Cl$ ratios measured by SIMS in these crystals differ by up to 0.38‰ (between Dur-B and Dur-C). The mapping results were filtered based on Confidence Index, and the black spots visible on the maps correspond to CI < 0.15. The black lines are most likely the polishing artefacts. [Colour figure can be viewed at wileyonlinelibrary.com]

The $\delta^{37}Cl$ measurements at the University of Delaware were performed in two measurement sessions a year apart using two different mass spectrometers and applying additional steps in the sample preparation procedure, which included an additional re-dissolution step of previously precipitated AgCl solids. The $10^3\delta^{37}Cl_{SMOC}$ values reported for these two sessions differ by only ~ 0.1, which confirm the high reproducibility of these measurements, suggesting the mass spectrometer has little or no effect on the data. Additionally, the sodium chloride isotopic reference material NIST SRM 975 was measured at the University of Delaware as a secondary quality control material (Appendix S5, Table S5.3). The mean $10^3\delta^{37}Cl_{SMOC}$ value for two

measurement sessions (+0.42 ± 0.04, 1*s*) agrees very well with the published $10^3\delta^{37}Cl_{SMOC}$ value of this reference sample (+0.43; Xiao *et al.* 2002).

Additional tests of the analytical procedures described above confirm the validity of our bulk methods and suggest that the variable offset between GS-IRMS laboratories results from apatite behaviour during the sample preparation. In general, an advantage of the used procedures is the fact that the chloride in all samples is in a pure silver chloride matrix which should (nearly) eliminate matrix effect issues during GS-IRMS measurements (Eggenkamp 1994). However, the samples that contain high sulfur mass fractions may

Table 5.
$\delta^{37}Cl_{SMOC}$ values determined by GS-IRMS for the apatite samples and isotopic reference material ISL-354

| Sample ID		MGMH #133648	TUBAF#38	TUBAF#40	MGMH #128441A	TUBAF#50	TUBAF#37	Dur	ISL-354[a]
Laboratory 1 at IPGP, dual-inlet mode, sample dissolution in 4.4 mol l^{-1} HNO$_3$									
$10^3\delta^{37}Cl_{SMOC}$ individual analyses	Aliquot 1	0.02 −0.03	0.04	−0.10 0.03 −0.04	0.23	0.09	0.03 −0.05	–	−0.15 0.11 0.16
	Aliquot 2	–	−0.03 −0.08	0.04 0.00	0.29 0.17	−0.12 0.06	–	–	−0.08 0.03 −0.03 −0.01 0.01 −0.14
Mean $10^3\delta^{37}Cl_{SMOC}$ (± 1s)		−0.01 ± 0.03	−0.02 ± 0.06	−0.01 ± 0.06	0.23 ± 0.06	0.01 ± 0.11	−0.01 ± 0.05	–	−0.01 ± 0.10
Laboratory 2 at University of Delaware, dual-inlet mode, sample dissolution in 0.5 mol l^{-1} HNO$_3$									
$10^3\delta^{37}Cl_{SMOC}$ individual analyses in 1st session	Aliquot 1	0.09 0.08	0.08 0.09	0.20 0.21	0.46 0.47	0.35 0.34	–	–	0.06 0.04
	Aliquot 2	−0.04 −0.04	0.03 0.03	0.27 0.27	0.47 0.48	0.37 0.38 0.37	–	–	0.03 0.03
	Aliquot 3	–	–	–	–	–	–	–	0.03 0.03
$10^3\delta^{37}Cl_{SMOC}$ individual analyses in 2nd session	Aliquot 4	0.16 0.14 0.15 0.14	0.00 0.01	0.19 0.18	0.35 0.34	–	0.16 0.18	0.19 0.18 0.18 0.16	0.13 0.13
	Aliquot 5	–	–	–	–	–	0.25 0.25 0.25 0.23	0.23 0.23 0.23 0.23	0.03 0.04 0.03 0.03 0.02
Mean $10^3\delta^{37}Cl_{SMOC}$ (± 1s)		0.09 ± 0.08	0.04 ± 0.04	0.22 ± 0.04	0.43 ± 0.06	0.36 ± 0.02	0.22 ± 0.04	0.20 ± 0.03	0.05 ± 0.04
Laboratory 3 at University of Texas, continuous-flow mode, pyrohydrolysis									
$10^3\delta^{37}Cl_{SMOC}$ individual analyses	Aliquot 1	−0.05	0.58	0.72	0.93	0.56	0.40	0.25 0.20	0.04
	Aliquot 2	0.51	0.29	0.60	0.42	0.77	0.27	0.03 0.19	−0.15
Mean $10^3\delta^{37}Cl_{SMOC}$ (± 1s)		0.23 ± 0.40	0.43 ± 0.20	0.66 ± 0.08	0.68 ± 0.36	0.66 ± 0.15	0.34 ± 0.09	0.17 ± 0.10	−0.05 ± 0.14
Summary of the GS-IRMS results									
Total number of measurements (n)		12	11	13	11	10	10	12	–
$10^3\delta^{37}Cl_{SMOC}$ working values (± 1s)[b]		0.09 ± 0.16	0.09 ± 0.19	0.20 ± 0.24	0.42 ± 0.20	0.32 ± 0.25	0.20 ± 0.13	0.19 ± 0.06	–
$^{37}Cl/^{35}Cl$ ratios[c]		0.319563	0.319563	0.319596	0.319667	0.319634	0.319596	0.319594	–

[a] The reference $10^3\delta^{37}Cl$ value for ISL-354 is +0.05 (Xiao *et al.* 2002).

[b] Simple mean of all individual $\delta^{37}Cl$ measurement results. Working values subject to future change as data generated by differing sample preparation become harmonised.

[c] The $^{37}Cl/^{35}Cl$ ratios were calculated using the absolute SMOC $^{37}Cl/^{35}Cl$ ratio of 0.319533 (zero point on the $\delta^{37}Cl_{SMOC}$ scale; see the third paragraph of Introduction for further details). These values have been further used for IMF calculations (Figure 10).

precipitate Ag$_2$S instead of AgCl when AgNO$_3$ is added to the solution. As a result, the AgCl yield could be lower but also (CH$_3$)$_2$S could be produced during the reaction with CH$_3$I, and this would impact the isotope ratio determination (Eggenkamp 2014). Two apatite samples TUBAF#37 and TUBAF#40 contain pyrite inclusions, which could not be fully removed from the split material (by mineral separation or hand-picking), and therefore, $\delta^{37}Cl$ determinations for these two specimens may have been impacted by Ag$_2$S precipitation. However, this could not be the case for other, sulfide-free samples (especially the inclusion-free TUBAF#50 specimen), which also show significant offsets between $\delta^{37}Cl$ values reported by different laboratories. Also, we could not correlate the variations of minor and trace elements (including SO$_4^{2-}$ in the apatite structure) detected by EPMA with variable offsets between GS-IRMS data sets. This further
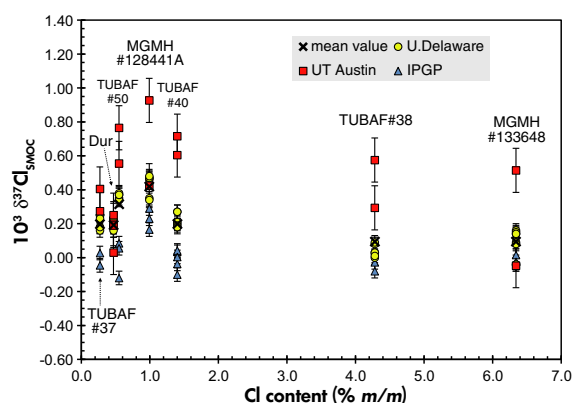
Figure 9. $\delta^{37}Cl_{SMOC}$ values determined independently in three GS-IRMS laboratories. The mean $10^3\delta^{37}Cl_{SMOC}$ values are within a range of +0.09 to +0.42 and do not correlate with apatite Cl mass fractions. A small bias can be seen between the laboratories. The error bars represent the uncertainties (1s) established during measurement sessions in each GS-IRMS laboratory. Continuous-flow IRMS determinations of $10^3\delta^{37}Cl$ are characterised by higher uncertainty of $\pm$ 0.13 (1s, UT Austin) and higher $10^3\delta^{37}Cl_{SMOC}$ values than those conducted in dual-inlet mode ($\pm$ 0.04, 1s, for both IPGP and U. Delaware). [Colour figure can be viewed at wileyonlinelibrary.com]

suggests more complex influence of chlorine extraction from apatite on the measured ratios and, more importantly, highlights the importance of the characterisation of reference materials for microanalysis with the support of multiple laboratories applying independent analytical protocols.

SIMS matrix effect and IMF

Matrix-dependent isotope mass fractionation is a common feature of isotopic studies of minerals crystallising as solid solutions (e.g., Śliwiński *et al.* 2016, Siron *et al.* 2017), and in most cases two or more reference materials should be used for defining the IMF correction factor in order to assess the presence of any such effect. In the study by Kusebauch *et al.* (2015a), it was noted that a matrix correction should be applied to SIMS measurements conducted on calcium phosphates of the apatite group, in which F can be extensively substituted by Cl and OH. The apatite samples characterised in our study cover nearly the entire spectrum of F-Cl-OH compositions (Figure 5). Based on our working values (Table 5) derived from GS-IRMS, the mean IMF value determined for the two endmembers TUBAF#37 and MGMH#133648 differs by ~ 0.24‰ (Figure 10a), which is significant when compared with the

small range of chlorine isotope ratios found in terrestrial materials, but it is rather negligible in view of larger variations of $\delta^{37}Cl$ values determined by different GS-IRMS laboratories and possible crystallographic orientation effect in SIMS analyses.

SIMS data collected on our six reference materials and corrected for IMF assuming a best-fit linear mass fraction dependency of IMF correspond well with $10^3\delta^{37}Cl$ values determined by GS-IRMS (Figure 10b). In contrast, the same SIMS data set corrected for IMF based on the analyses of the single fragment of Dur fluorapatite shows systematic offsets from the data reported by GS-IRMS (Figure 10c). The highest offsets were recorded for the two chlorapatite samples MGMH#133648 and TUBAF#38, for which $10^3\delta^{37}Cl$ values obtained using SIMS were +0.10 (based on a linear correction of IMF) vs. -0.34 (when IMF correction was based on Dur only) for MGMH#133648, and +0.11 (based on a linear correction) vs. -0.22 (Dur correction) for TUBAF#38. GS-IRMS analyses yielded recommended $10^3\delta^{37}Cl$ values of +0.09 for both chlorapatite specimens.

The SIMS IMF value of the Dur fluorapatite is slightly higher (by ~ 0.2%) than IMF factors of other Cl-poor samples, which may contain a contribution from the observed crystallographic orientation effect; this IMF value was determined based on the measurements conducted on a single fragment of the Dur crystal (Dur-1 in mount #1), which was used for monitoring of the instrumental drift during the SIMS homogeneity test. Alternatively, a slightly different IMF may be a characteristic feature of Dur apatite. A higher IMF value for Dur was also noted in the additional test of selected crystals of TUBAF#37 and TUBAF#38 embedded in mount #2. In that case, the IMF value for a single crystal of Dur (Dur-2) was higher by 0.16‰ than a mean value for multiple crystals of TUBAF#37-B. The reason for IMF variations between RMs having low Cl mass fractions ($\leq$ 1.4% *m/m*) is uncertain at the moment. Crystallographic orientation effect can be one of the reasons, but a variable offset between individual data sets generated in three independent GS-IRMS laboratories may also play a role here. Therefore, we recommend using multiple, randomly oriented fragments of at least two RMs to account for crystallographic orientation effect on collected $^{37}Cl/^{35}Cl$ ratios, thereby reducing the risk of potential bias associated with conventional $\delta^{37}Cl$ determinations. Application of such an approach improved quality and validated the SIMS data in the previous study by Wudarska *et al.* (2020), in which the data reduction was conducted using four RMs.

Furthermore, the IMF calibration based on apatite reference materials closely matching the composition of the
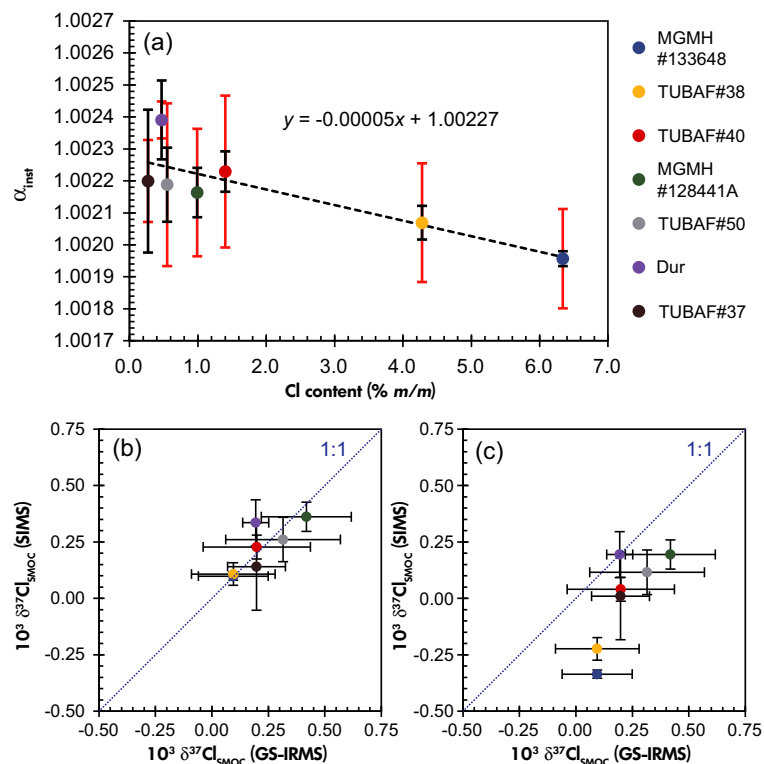
Figure 10. (a) The correlation of α_{inst} with Cl mass fraction is visible along apatite solid solution series shifting by ~ 0.24–0.30‰. The black bars represent total uncertainty of the SIMS measurements (uncertainties of individual analyses and repeatability during homogeneity test, see Figure 6). The red bars represent 1 standard deviation of all $\delta^{37}Cl_{SMOC}$ determinations by GS-IRMS. Dashed line represents the best-fit line to all data, including the data from the single fragment of Dur apatite. (b) Comparison of mean $10^3\delta^{37}Cl$ values determined by GS-IRMS with calculated SIMS values corrected for IMF assuming a linear mass fraction dependency of IMF (dashed line and the equation in the graph a). (c) Comparison of mean $10^3\delta^{37}Cl$ values determined by GS-IRMS with calculated SIMS values corrected for IMF based only on the data from the single fragment of Dur. [Colour figure can be viewed at wileyonlinelibrary.com]

unknown samples would not only minimise the matrix effect but also enable the use of the analytical protocols tailored to the materials being studied. In the case where Cl-poor samples are analysed along with a RM having much higher Cl content, the current of primary ion beam should be limited to avoid too high ion counting rates for Faraday cups during RM measurements. Consequentially, measurement precision for the unknowns must be worse than that in the case where the applied primary ion beam current is optimised to the unknowns. In this study, all specimens were tested under the identical conditions, and therefore, the measurements yielded better counting statistics and repeatability for Cl-rich samples (Figure 6).

Conclusions

Metrological splits of the apatite samples described here can be obtained through the IAGeo Limited website (www.ia geo.com). The $10^3\delta^{37}Cl$ working values are as follows:

MGMH#133648 = +0.09 ± 0.16 (1s), TUBAF#38 = + 0.09 ± 0.19, TUBAF#40 = +0.20 ± 0.24, MGMH# 128441A = +0.42 ± 0.20, TUBAF#50 = +0.32 ± 0.25, TUBAF#37 = +0.20 ± 0.13. All six reference materials are suitable for calibration of the in situ $\delta^{37}Cl$ measurements. We recommend collecting BSE and reflected-light optical images of mounted polished crystals prior to isotopic analyses in order to avoid any possible inclusions and any crust that might be present. We also advise using MGMH#133648 and TUBAF#38 with caution for chlorine abundance determinations due to possible variations of Cl/OH ratio distribution in these two specific chlorapatite specimens. Taking into consideration a potential crystal orientation effect on measured $^{37}Cl/^{35}Cl$ ratios and matrix-dependent IMF, our recommendation for future SIMS-based $\delta^{37}Cl_{SMOC}$ determinations on minerals from the apatite group is to use multiple fragments of (at least two, but preferably three) reference materials matching as closely as possible the Cl content of the unknown samples. Due to the

GEOSTANDARDS and GEOANALYTICAL RESEARCH

offset between $10^3\delta^{37}$Cl values determined in three GS-IRMS laboratories, when interpreting SIMS data we recommend taking into account that the total uncertainty of SIMS results based on our reference samples would be at the level of $\pm \sim 0.3$, despite better capabilities offered by large-geometry SIMS instruments.

Acknowledgements

Conflicts of interest

The authors declare they have no conflicts of interest.

Data availability statement

The data that support the findings of this study are available in the supplementary material and from the corresponding author upon request.

References

Bellucci J.J., Whitehouse M.J., John T., Nemchin A.A., Snape J.F., Bland P.A. and Benedix G.K. (2017)
Halogen and Cl isotopic systematics in Martian phosphates: implications for the Cl cycle and surface halogen reservoirs on Mars. Earth and Planetary Science Letters, 458, 192–202.

Bonifacie M., Jendrzejewski N., Agrinier P., Coleman M., Pineau F. and Javoy M. (2007)
Pyrohydrolysis-IRMS determination of silicate chlorine stable isotope compositions. Application to oceanic crust and meteorite samples. Chemical Geology, 242, 187–201.

Bouvier A.-S. and Baumgartner L. (2013)
New method for precise Cl isotopes measurement by SIMS. Mineralogical Magazine, 77, 753.

Boyce J.W., Treiman A.H., Guan Y., Ma C., Eiler J.M., Gross J., Greenwood J.P. and Stolper E.M. (2015)
The chlorine isotope fingerprint of the lunar magma ocean. Science Advances, 1, e1500380.

Brand W.A., Coplen T.B., Vogl J., Rosner M. and Prohaska T. (2014)
Assessment of international reference materials for isotope-ratio analysis (IUPAC Technical Report). Pure and Applied Chemistry, 86, 425–467.

Coplen T.B. (2011)
Guidelines and recommended terms for expression of stable-isotope-ratio and gas-ratio measurement results. Rapid Communications in Mass Spectrometry, 25, 2538–2560.

Eggenkamp H.G.M. (1994)
δ^{37}Cl the geochemistry of chlorine isotopes. Geologica Ultraiectina, 116, 150.

Eggenkamp H. (2014)
The geochemistry of stable chlorine and bromine isotopes. Springer (Berlin/Heidelberg), 172pp.

Eggenkamp H., Bonifacie M., Ader M. and Agrinier P. (2016)
Experimental determination of stable chlorine and bromine isotope fractionation during precipitation of salt from a saturated solution. Chemical Geology, 433, 46–56.

Eggenkamp H.G.M., Louvat P., Agrinier P., Bonifacie M., Bekker A., Griffioen J., Horita J., Brocks J.J. and Bagheri R. (2019)
The bromine and chlorine isotope composition of primary halite deposits and its consequence for the historical isotope composition of seawater. Geochimica et Cosmochimica Acta, 264, 13–29.

Godon A., Jendrzejewski N., Eggenkamp H.G.M., Banks D.A., Ader M., Coleman M.L. and Pineau F. (2004)
A cross-calibration of chlorine isotopic measurements and suitability of seawater as the international reference material. Chemical Geology, 207, 1–12.

Goldoff B., Webster J.D. and Harlov D.E. (2012)
Characterization of fluor-chlorapatites by electron probe microanalysis with a focus on time-dependent intensity variation of halogens. American Mineralogist, 97, 1103–1115.

Gonfiantini R., Tonarini S., Gröning M., Adorni-Braccesi A., Al-Ammar A.S., Astner M., Bächler S., Barnes R.M., Bassett R.L., Cocherie A., Deyhle A., Dini A., Ferrara G., Gaillardet J., Grimm J., Guerrot C., Krähenbühl U., Layne G., Lemarchand D., Meixner A., Northington D.J., Pennisi M., Reitznerová E., Rodushkin I., Sugiura N., Surberg R., Tonn S., Wiedenbeck M., Wunderli S., Xiao Y. and Zack T. (2003)
Intercomparison of boron isotope and concentration measurements. Part II: Evaluation of results. Geostandards Newsletter: the Journal of Geostandards and Geoanalysis, 27, 41–57.

Harlov D. and Förster H.-J. (2003)
Fluid-induced nucleation of (Y+REE)-phosphate minerals within apatite: nature and experiment. Part II. Fluorapatite. American Mineralogist, 88, 1209–1229.

references

Holt B.D., Sturchio N.C., Abrajano T.A. and Heraty L.J. (1997)
Conversion of chlorinated organic compounds to carbon dioxide and methyl chloride for isotopic analysis of carbon and chlorine. Analytical Chemistry, 69, 2727–2733.

Huberty J.M., Kita N.T., Kozdon R., Heck P.R., Fournelle J.H., Spicuzza M.J., Xu H. and Valley J.W. (2010)
Crystal orientation effects in $\delta^{18}O$ for magnetite and hematite by SIMS. Chemical Geology, 276, 269–283.

Hughes J.M., Harlov D., Kelly S.R., Rakovan J. and Wilke M. (2016)
Solid solution in the apatite OH-Cl binary system: compositional dependence of solid-solution mechanisms in calcium phosphate apatites along the Cl-OH binary. American Mineralogist, 101, 1783–1791.

Hughes J.M. and Rakovan J. (2002)
The crystal structure of apatite, $Ca_5(PO_4)_3(F, OH, Cl)$. Reviews in Mineralogy and Geochemistry, 48, 1–12.

John T., Layne G.D., Haase K.M. and Barnes J.D. (2010)
Chlorine isotope evidence for crustal recycling into the Earth's mantle. Earth and Planetary Science Letters, 298, 175–182.

Ketcham R.A. (2015)
Calculation of stoichiometry from EMP data for apatite and other phases with mixing on monovalent anion sites. American Mineralogist, 100, 1620–1623.

Kita N.T., Huberty J.M., Kozdon R., Beard B.L. and Valley J.W. (2011)
High-precision SIMS oxygen, sulfur and iron stable isotope analyses of geological materials: accuracy, surface topography and crystal orientation. Surface and Interface Analysis, 43, 427–431.

Kusebauch C., John T., Barnes J.D., Klügel A. and Austrheim H.O. (2015c)
Halogen element and stable chlorine isotope fractionation caused by fluid–rock interaction (Bamble Sector, SE Norway). Journal of Petrology, 56, 299–324.

Kusebauch C., John T., Whitehouse M.J. and Engvik A.K. (2015a)
Apatite as probe for the halogen composition of metamorphic fluids (Bamble Sector, SE Norway). Contributions to Mineralogy and Petrology, 170, 34.

Kusebauch C., John T., Whitehouse M.J., Klemme S. and Putnis A. (2015b)
Distribution of halogens between fluid and apatite during fluid-mediated replacement processes. Geochimica et Cosmochimica Acta, 170, 225–246.

Layne G.D., Godon A., Webster J.D. and Bach W. (2004)
Secondary ion mass spectrometry for the determination of $\delta^{37}Cl$: Part I. Ion microprobe analysis of glasses and fluids. Chemical Geology, 207, 277–289.

Li L., Bonifacie M., Aubaud C., Crispi O., Dessert C. and Agrinier P. (2015)
Chlorine isotopes of thermal springs in arc volcanoes for tracing shallow magmatic activity. Earth and Planetary Science Letters, 413, 101–110.

Li Y., Li Q.-L., Tang G.-Q., Gargano A., Sharp Z., Pitawala A., Zhao L., Zhai M.-G. and Li X.-H. (2020)
Eppawala-AP, Sri Lanka, an apatite reference material for high precision chlorine isotope analysis. Atomic Spectroscopy, 41, 51–56.

Manzini M., Bouvier A.-S., Barnes J.D., Bonifacie M., Rose-Koga E.F., Ulmer P., Métrich N., Bardoux G., Williams J., Layne G.D., Straub S., Baumgartner L.P. and John T. (2017)
SIMS chlorine isotope analyses in melt inclusions from arc settings. Chemical Geology, 449, 112–122.

Marks M.A.W., Wenzel T., Whitehouse M.J., Loose M., Zack T., Barth M., Worgard L., Krasz V., Eby G.N., Stosnach H. and Markl G. (2012)
The volatile inventory (F, Cl, Br, S, C) of magmatic apatite: an integrated analytical approach. Chemical Geology, 291, 241–255.

McDowell F.W., McIntosh W.C. and Farley K.A. (2005)
A precise $^{40}Ar–^{39}Ar$ reference age for the Durango apatite (U–Th)/He and fission-track dating standard. Chemical Geology, 214, 249–263.

Meisel T.C. (2019)
Why δ is not‰ and why we should not use ϵ and μ notations. Geostandards and Geoanalytical Research, 43, 527–528.

Pan Y. and Fleet M.E. (2002)
Compositions of the apatite-group minerals: substitution mechanisms and controlling factors. Reviews in Mineralogy and Geochemistry, 48, 13–49.

Potts N.J., Barnes J.J., Tartèse R., Franchi I.A. and Anand M. (2018)
Chlorine isotopic compositions of apatite in Apollo 14 rocks: evidence for widespread vapor-phase metasomatism on the lunar nearside ~ 4 billion years ago. Geochimica et Cosmochimica Acta, 230, 46–59.

Sarafian A.R., John T., Roszjar J. and Whitehouse M.J. (2017)
Chlorine and hydrogen degassing in Vesta's magma ocean. Earth and Planetary Science Letters, 459, 311–319.

Schnetger B. and Muramatsu Y. (1996)
Determination of halogens, with special reference to iodine, in geological and biological samples using pyrohydrolysis for preparation and inductively coupled plasma-mass spectrometry and ion chromatography for measurement. Analyst, 121, 1627–1631.

Sharp Z.D., Barnes J.D., Brearley A.J., Chaussidon M., Fischer T.P. and Kamenetsky V.S. (2007)
Chlorine isotope homogeneity of the mantle, crust and carbonaceous chondrites. Nature, 446, 1062–1065.

references

Sharp Z.D., Shearer C.K., McKeegan K.D., Barnes J.D. and Wang Y.Q. (2010)
The chlorine isotope composition of the moon and implications for an anhydrous mantle. Science, 329, 1050–1053.

Sharp Z., Williams J., Shearer C., Agee C. and McKeegan K. (2016)
The chlorine isotope composition of Martian meteorites 2. Implications for the early solar system and the formation of Mars. Meteoritics and Planetary Science, 51, 2111–2126.

Shields W.R., Garner E.L. and Dibeler V.H. (1963)
Absolute isotopic abundance ratio and the atomic weight of chlorine. In: Elliott R.M. (ed.), Advances in mass spectrometry, Volume 2. Pergamon (Glasgow), 163–173.

Shimizu K., Suzuki K., Saitoh M., Konno U., Kawagucci S. and Ueno Y. (2015)
Simultaneous determinations of fluorine, chlorine, and sulfur in rock samples by ion chromatography combined with pyrohydrolysis. Geochemical Journal, 49, 113–124.

Siron G., Baumgartner L., Bouvier A.-S., Putlitz B. and Vennemann T. (2017)
Biotite reference materials for secondary ion mass spectrometry $^{18}O/^{16}O$ measurements. Geostandards and Geoanalytical Research, 41, 243–253.

Śliwiński M.G., Kitajima K., Kozdon R., Spicuzza M.J., Fournelle J.H., Denny A. and Valley J.W. (2016)
Secondary ion mass spectrometry bias on isotope ratios in dolomite–ankerite, part I: $\delta^{18}O$ matrix effects. Geostandards and Geoanalytical Research, 40, 157–172.

Stephant A., Anand M., Zhao X., Chan Q., Bonifacie M. and Franchi I. (2019)
The chlorine isotopic composition of the Moon: insights from melt inclusions. Earth and Planetary Science Letters, 523, 115715.

Stock M.J., Humphreys M.C.S., Smith V.C., Johnson R.D., Pyle D.M. and EIMF (2015)
New constraints on electron-beam induced halogen migration in apatite. American Mineralogist, 100, 281–293.

Stormer J.C., Pierson M.L. and Tacker R.C. (1993)
Variation of F and Cl X-ray intensity due to anisotropic diffusion in apatite during electron microprobe analysis. American Mineralogist, 78, 641–648.

Tartèse R., Anand M., Joy K.H. and Franchi I.A. (2014)
H and Cl isotope systematics of apatite in brecciated lunar meteorites Northwest Africa 4472, Northwest Africa 773, Sayh al Uhaymir 169, and Kalahari 009. Meteoritics and Planetary Science, 49, 2266–2289.

Teiber H., Marks M.A.W., Arzamastsev A.A., Wenzel T. and Markl G. (2015)
Compositional variation in apatite from various host rocks: clues with regards to source composition and crystallization conditions. Journal of Mineralogy and Geochemistry, 192, 151–167.

Treiman A.H., Boyce J.W., Gross J., Guan Y., Eiler J.M. and Stolper E.M. (2014)
Phosphate-halogen metasomatism of lunar granulite 79215: impact-induced fractionation of volatiles and incompatible elements. American Mineralogist, 99, 1860–1870.

Wang Y., Hsu W. and Guan Y. (2019)
An extremely heavy chlorine reservoir in the Moon: insights from the apatite in lunar meteorites. Scientific Reports, 9, 5727.

Wei H.-Z., Jiang S.-Y., Xiao Y.-K., Wang J., Lu H., Wu B., Wu H.-P., Li Q. and Luo C.-G. (2012)
Precise determination of the absolute isotopic abundance ratio and the atomic weight of chlorine in three international reference materials by the positive thermal ionization mass spectrometer-Cs_2Cl^+-graphite method. Analytical Chemistry, 84, 10350–10358.

Wudarska A., Słaby E., Wiedenbeck M., Birski Ł., Wirth R., Götze J., Lepland A., Kusebauch C. and Kocjan I. (2020)
Chlorine isotope composition of apatite from the >3.7 Ga Isua Supracrustal Belt, SW Greenland. Minerals, 10, 27.

Xiao Y.K., Yinming Z., Qingzhong W., Haizhen W., Weiguo L and Eastoe C.J. (2002)
A secondary isotopic reference material of chlorine from selected seawater. Chemical Geology, 182, 655–661.

Supporting information

The following supporting information may be found in the online version of this article:

Appendix S1. Backscattered electron images of the apatite fragments.

Appendix S2. Images of four of the sample mounts.

Appendix S3. The spectral lines, corresponding peak counting times, and the calibration materials used for major and trace elements determination by EPMA.

Appendix S4. Topographic model of a typical SIMS crater.

Appendix S5. Additional GS-IRMS data tables and information.

Appendix S6. Complete EPMA data tables (5 nA and 40 nA).

Appendix S7. Complete SIMS data tables.

This material is available as part of the online article from: http://onlinelibrary.wiley.com/doi/10.1111/ggr.12366/abstract (This link will take you to the article abstract).